Public

Report

Document ID	Version	Status	Reg no	Page
1411328	2.0	Approved		1 (54)
Author C. Müller T. Heckel P. Brömel M. Pavlovic U. Ronneteg			Date 2014-02-07	
Reviewed by Sabina Hammarberg (QA)			Reviewed date 2014-02-25	
Approved by Jan Sarnet			Approved date 2014-02-25	

Attenuation dependent detectability at ultrasonic inspection of copper

Summary

This report describes the progress in understanding and describing the detectability of the ultrasonic inspection technique developed by SKB for the inspection of copper tubes used for the final disposal of the Swedish spent nuclear fuel. In former research activities dedicated to the different parts of the canister, the probability of detection (POD) evaluation technique, as developed for thin aircraft components, was further developed for the application on complex thick-walled components. The result of this development was the introduction of a "multi-parameter" POD framework. In contrast to taking only the defect size into consideration (as for aircraft components) additional influencing factors, relevant for thick components, such as depth position, orientation and part geometry, were included. Furthermore, the variation of ultrasonic attenuation due to various material properties was included.

The aim of the underlying investigation was to achieve a deeper insight into the effect of attenuation on the detectability of defects at larger depths in the copper tube. For this purpose, test samples with different level of attenuated material, containing flat bottom holes of various sizes, were manufactured. The samples were then inspected by the phased array ultrasonic technique developed by SKB. The results, including the amplitudes from the flat bottom holes and the multiple back wall echoes, as well as the frequency domain for both the surface and back wall echoes, were used as input for the POD calculations.

The data analysis showed that the attenuation and the low pass filtering of the ultrasonic signal, due to variations in the grain structure, varied along both the surface and the depth of the tubes. As a consequence, the difference between the second and the first back wall echoes were not sufficient to determine the local attenuation, which affects the signal response from the individual defect. These deviations were taken into account by manual adaption of the modelled data.

The results for the final attenuation are in good agreement with former investigations of the attenuation in copper tubes and the POD results have been verified by conventional POD calculations without any model assumptions included. The detectable flat bottom hole sizes, as represented by the corresponding d90/95 values, vary from less than 2 mm for low attenuated material up to 4 mm for

Svensk Kärnbränslehantering AB
Swedish Nuclear Fuel and Waste Management Co
PO Box 925, SE-572 29 Oskarshamn
Visiting address Gröndalsgatan 15
Phone +46-491-76 79 00 Fax +46-491-76 79 30
www.skb.se
556175-2014 Seat Stockholm

high attenuated material. This indicates that the developed ultrasonic technique is well suitable for inspection of copper tubes with attenuation up to the level of the investigated material.

Table of Contents

1 Introduction

Over the years, SKB has developed processes to manufacture copper tubes by extrusion and pierce and draw techniques (SKB 2010). As a tool in the development process all manufactured tubes have been inspected by mechanized phased array ultrasonic technique. Results from these inspections have shown variations in ultrasonic attenuation within and between manufactured tubes that indicate variations in the material structure.

Within the scope of the NDT Reliability project, BAM (Federal Institute for Materials Research and Testing) formulated a methodology to determine the detectability of the developed phased array ultrasonic inspection techniques by calculation of Probability of Detection (POD) curves. This report presents the work that has been conducted in order to investigate how the variations in attenuation affect the detectability. The main work has been focused on development of a methodology for calculation of POD-curves customized to the phased array ultrasonic inspection techniques developed by SKB and its application of the inhomogeneous attenuating copper tubes.

The results from these investigations will be used together with parallel metallographic investigations performed on samples of copper tube material with the same origin as in this study.

2 Reliability

During the second European American Workshop on NDE Reliability, held in 1999 in Boulder, Colorado, USA (ASNT 1999), **the NDE System** was defined as the procedure, equipment and personnel that are used in performing NDE inspection and **the NDE reliability** as the degree that an NDT system is capable of achieving its purpose regarding detection, characterization and false calls. These definitions were taken as the basis for this reliability investigation. The focus of this reliability investigation lies on the defect detection under different conditions. The probability of detecting critical defects multiplied with the probability of occurrence of those defects yields the probability of canister leakage, caused by defects from the manufacturing.

2.1 Conventional POD

Considering the capability of the NDT-system to detect a defect, it has to be taken into account that the defects of the same size will not always be detected and, therefore, might result in different detection probabilities (Berens 1989). Due to this uncertainty, the detection capability has to be expressed in terms of a probability, i.e. the probability of detection (POD) as a function of defect size. Due to the detection of defects being based on the evaluation of digitized signals in the mechanized inspections in the underlying project, the signal response POD was the selected approach. A schematic representation of the basic principles of the signal response POD is depicted in Figure 2-1.

A defect of size *a* causes a signal with amplitude *â*. When the signal is above a selected threshold, it is counted as a defect indication and otherwise as noise. The *â* versus *a* curve, in almost all cases on a logarithmic scale (the relation depends on the physical law which predicts the *â* to be a function of *a,* e.g. the radiographic absorption law or the ultrasonic reflectivity) is indicated on the lower left hand side of Figure 2-1. Using an appropriate statistical model for the data distribution, as developed by Berens (1989), this diagram can be transformed into a typical POD curve with a corresponding 95% lower confidence bound.

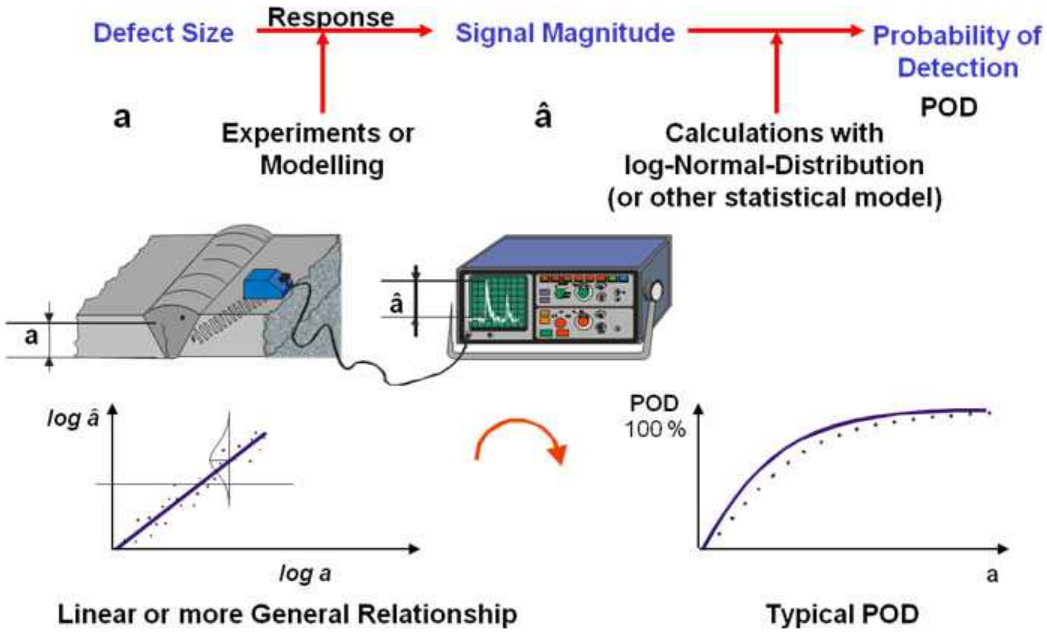

Figure 2-1. *Signal response POD principle.*

The conventional signal response analysis designates the measured response signals as *â* and the crack depth or any other defect dimension responsible for the signal strength as *a*. The crack depth *a* is considered to be the real crack depth, i.e. the truth, and the measured peak amplitude as a perceived depth (hence the designation *â*). Values are then plotted against each other in a so called *â* vs. *a* diagram. One should not forget that the crack depth also originates from the geometrical measurement, so this diagram could also be seen as a comparison of two measurements – NDT vs. geometrical. Of course, the precision of geometrical measurement is on several orders of magnitude better than that of the NDT systems and can be considered as the truth for all practical applications.

In the next step linearity between the data is observed in the *â* vs. *a* log-log diagram. This is the model that describes how the signal changes with the crack depth - linearly in a logarithmic scale. It is important to notice here that this model comes from the pure observation of the data, as stated by Berens (1989). That means that even if this model has been proven to be valid for the crack data and the eddy current system described in the paper, it does NOT mean that it is valid for any other defects and inspection systems! Even if one observes linear behaviour of the data, it does not mean that the flaw size is the sole cause of this behaviour. Some other factor could influence the data in a way so that there only appears to be a linear relationship between the response signal and the size of the flaw. This is especially true for the NDT data which as a rule comes in small sample sizes.

The POD is then calculated by setting the decision threshold and assuming the scatter of the peak signal measurements to be normally distributed around the model curve (line). Then the part of the cumulative distribution function that is above the threshold equals the POD for one specific defect size. This is repeated for every defect size in the observed range and the POD curve is constructed. Figure 2-2 shows a typical result using the *â* versus *a* scheme as explained above. The indicated vertical line shows the a90/95 value where the lower 95% confidence limit crosses the 90% POD level, i.e. in 95 from 100 repetitions the POD for this defect size would be above 90% and the defects above this size are considered to be detected with certainty. This concept was developed within the frame of aerospace applications. When applying this approach to industrial applications, such as the copper canister components for radioactive spent fuel, it needs to be expanded to real industrial conditions.

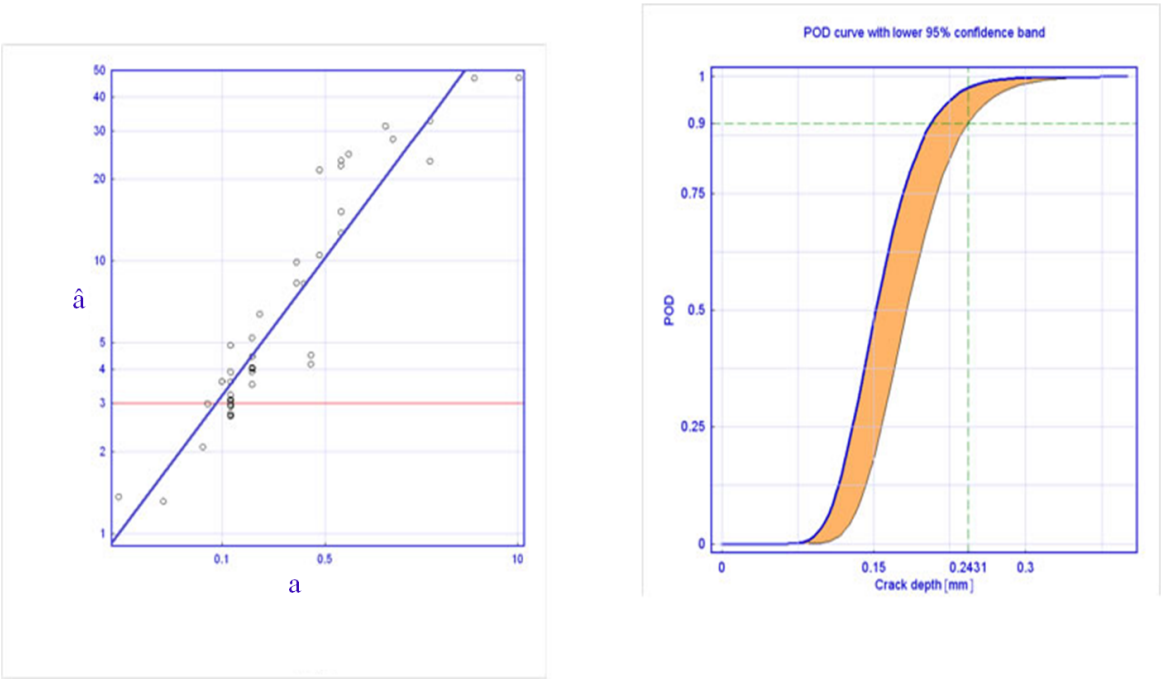

Figure 2-2. *Typical signal response POD â versus a diagram on the left hand side and the resulting POD as a function of defect parameter size on the right hand side.*

2.2 Multi-parameter POD

As described before, the conventional model expresses the POD as a function of one influencing parameter. In most of the cases, this is considered to be the size of the defect. If there is some other influencing parameter, one could plot the signal response against the value of that parameter and if the linearity is observed the POD could be calculated in the same way. In case the sample size is small, special care should be taken to interpret linearity in the relation between signal height and the parameter. In this case it his helpful to verify the relation with the physical model behind it.

Furthermore, if there is more than just one parameter that influences the POD, one could create several POD diagrams for every parameter and for every combination of the values of parameters. For instance, in the case of flat bottom holes the amplitude, and hence the POD, is proportional to the square of the diameter and reciprocally to the depth of it in the far field region. To carry out the necessary number of experiments is practically impossible, especially with the increase of the number of influencing parameters.

In this situation a multi-parameter model finds its application. The measured signal is plotted against the theoretically calculated one, which represents the optimal manner to combine the influencing parameters. So this diagram could be called “Measured vs. modelled response amplitude” and it is in the first instance a validation of the model. In an ideal case, if all influencing parameters are included in the model, all points would lie on a 45 degrees inclined line. However, in real applications it is not possible to include all influencing parameters. Therefore only those parameters that influence the response signal the most essential parameters, defined in ENIQ (2005), are selected. The observed scatter of measured signals comes from all other influencing parameters that are not included in the model. The reason why we call it a multi-parameter *a* is because the model gives us a function how this amplitude depends on the influencing parameters.

The POD is calculated from the scatter of the measured signals for each value of a modelled signal in the observed range. This is done in exactly the same way as in the conventional model - by setting a threshold and assuming normally distributed signal scatter and calculating the part of the cumulative distribution function that is above the threshold. This is the POD as a function of multi-parameter *a,* which could be called theoretical response signal. Since the theoretical model (simulation) gives the relationship between this response signal and the influencing parameters, it is now possible to calculate the POD curve as a function of all of the parameters in determining the value of a for this combination and assign POD (a) and the corresponding confidence limit to it.

As opposed to the conventional model, in which the linearity between the signal and the influencing parameter is assumed just by **observing** one set of data, the relationship between the response signal and influencing parameters in the multi-parameter model comes from the **simulation** representing our understanding of the underlying physics of the inspection process (in our case: propagation of ultrasonic waves in elastic materials). In both cases, the confidence bounds are calculated from the measurement (which is directly influenced by the sample size and scatter of the data). The confidence bounds express the uncertainty of the system which can only be determined on the of basis true-measured data (in contrast to simulated data) as described by Pavlovic et al. (2012).

Specifically, for the purposes of the current “NDT-reliability project” there is a need for a multi-parameter *a*, where the depth, size and orientation of the defect, as well as the variable attenuation of the material, which can occur in the bulk canister components, can be taken into account. To investigate this, a model assisted multi-parameter methodology (Pavlovic et al. 2008, 2009, 2012) was developed and applied to the lid of the copper canister. The POD as a function of defect size in the form of a flat bottom hole (FBH) diameter, depth and angle is presented in Figure 2-3 (a), (b) and (c), respectively (Pavlovic et al. 2009). The sharp decrease of POD with increasing angle, for example, shows how important a comprehensive multi-parameter consideration is.

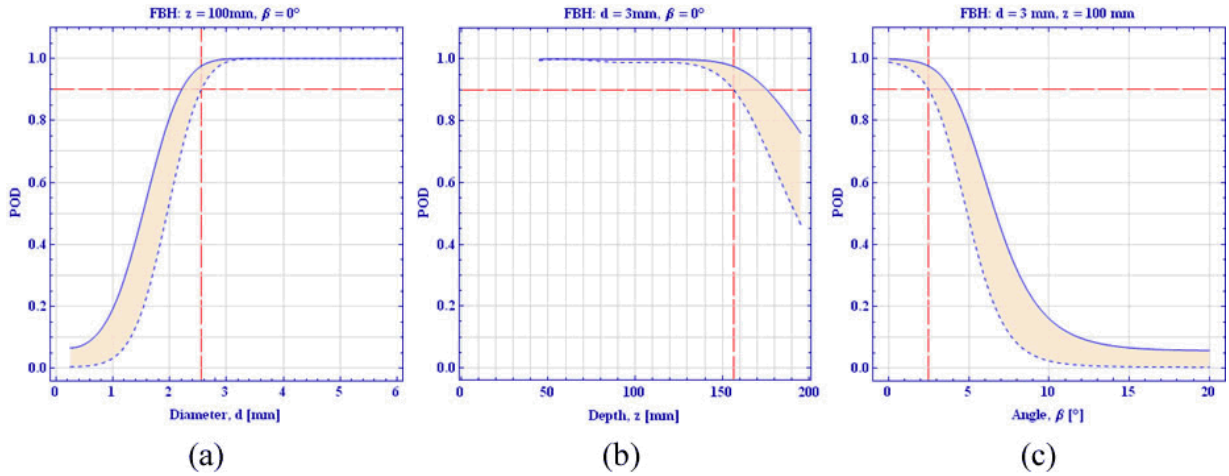

***Figure 2-3**. Decomposed multi-parameter POD.*

As described above, the mathematical procedure of the multi-parameter POD relies on applying the Berens algorithm (Berens 1989) to the "signal as a function of a MP (a multi-parameter) instead of to the signal as a function of defect size. This procedure provides for the a an optimal combination of all intrinsic influencing parameters in terms of the theoretically modelled signal amplitude. Consequently – in case the applied model is appropriate – the $\hat{a}$ versus a curve would always be a 45° line and the scatter of the individual points originate from the system noise.

After the multi-parameter POD is established, it can be decomposed to the individual dependencies on depth, diameter etc. However, the carrier of information about the system behaviour is the MP-POD-curve, from which the data are derived. The big advantage of this comprehensive approach is that the physics of the system – in our case focused phased array ultrasonic system – is considered accurately, which would not be the case when only applying an empirical Berens-POD (the so-called POD0 approach).

3 Ultrasonic inspection technique

The ultrasonic inspection (UT11) of the copper tube is performed by mechanized data collection using a stepwise helicoil inspection sequence, i.e. the tube rotates one full revolution and then moves forward in axial direction by 113 mm (see Figure 3-1). The ultrasonic system consists of a Dynaray phased array equipment together with the UltraVision software, a linear array probe (Table 3-1), a probe fixture with an integrated local immersion tank and a manipulator for rotation of the tube and axial movement probe. The array is positioned along the axial direction of the tube with a water path of about 30 mm. The inspection is performed by collection of data for each millimetre with the use of two ultrasonic channels for different inspection depths according to Table 3-2 to Table 3-4.

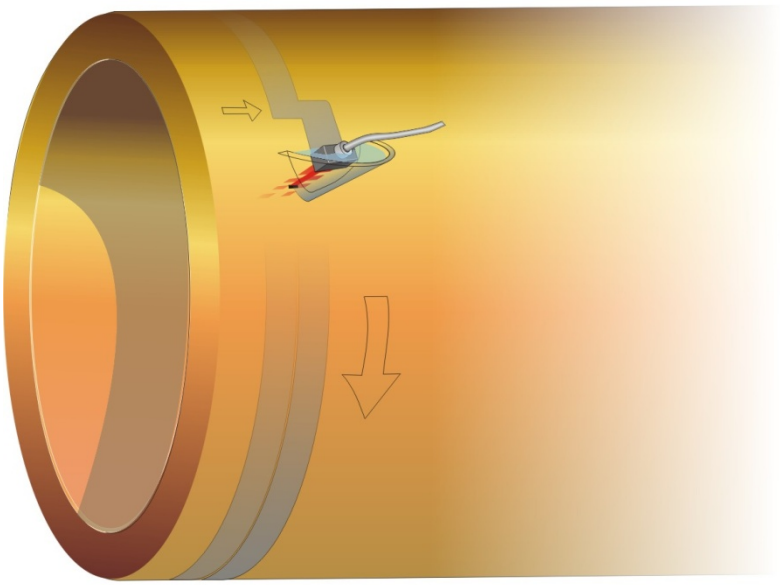

Figure 3-1. *Ultrasonic scanning sequence.*

Table 3-1. Phased array probe used for inspection of copper components.

Centre frequency (MHz)	Array geometry	Number of elements	Inter elements pitch (mm)	Inter elements space (mm)	Width of the elements (mm)
3.5	Linear	128	1.0	0.15	16.0

Table 3-2. General ultrasonic settings

Sound velocity (m/s)	Water path (mm)	Pulse width (NS)	Pulse voltage (V)	Digitizing frequency (MHz)	Recurrence (Hz)	Compression	Digital converter (Bit)
4700	30	140	90	100	2000	6	16

Table 3-3. Specific ultrasonic settings

Channel	Inspection range (mm)	Beam angle in the material (°)	Focal point (mm)	No. of elements	No. of focal laws
FD10 12elts	0-20	0	10	12	117
FD40 16elts	20-55	0	40	16	113

Table 3-4. TGC settings

Channel FD10 12elts		Channel FD40 16elts	
Depth (mm)	**Gain (dB)**	**Depth (mm)**	**Gain (dB)**
1.03	0.0	1.03	0.0
4.98	0.0	24.91	1.0
9.96	2.0	39.95	4.0
19.93	4.5	47.94	5.5

4 Test objects

Three segments from three different copper tubes, T53 (axial segment 0-1485 mm), T58 (axial segment 3530-4850 mm) and T64 (axial segment 2170-4260 mm) with outer diameter of 960 mm and material thickness of 54 mm, have been chosen based on their difference in ultrasonic attenuation. In the extruded tube T53 flat bottom holes (FBH) have been drilled in one reference area with low attenuation and in one area with higher attenuation (see Figure 4-1). In the extruded tube T58 (Figure 4-2) and in the Tube T64 (Figure 4-3), manufactured by a pierce and draw process, flat bottom holes have been drilled in areas with high attenuation. In each of the four areas nine 5 mm deep flat bottom holes have been drilled according Table 4-1. All flat bottom bore holes were located at the depth of 49 mm measured from the outer surface.

Table 4-1. Drilled holes in the copper tube segments

Tube segment	Flat bottom hole. Diameter (mm) and circumferential (°) / axial (mm) position								
	1.0	1.5	2.0	2.5	3.0	3.5	4.0	5.0	6.0
T53 low attenuation	240/ 1320	235/ 1320	230/ 1320	225/ 1320	220/ 1320	215/ 1320	210/ 1320	205/ 1320	200/ 1320
T53 high attenuation	125/ 1240	168/ 1240	125/ 1280	168/ 1320	125/ 1320	168/ 1360	125/ 1360	168/ 1400	125/ 1400
T58 high attenuation	245/ 3650	240/ 3650	235/ 3650	230/ 3650	225/ 3650	220/ 3650	215/ 3650	210/ 3650	205/ 3650
T64 high attenuation	170/ 4180	165/ 4180	160/ 4180	155/ 4180	150/ 4180	145/ 4180	140/ 4180	135/ 4180	130/ 4180

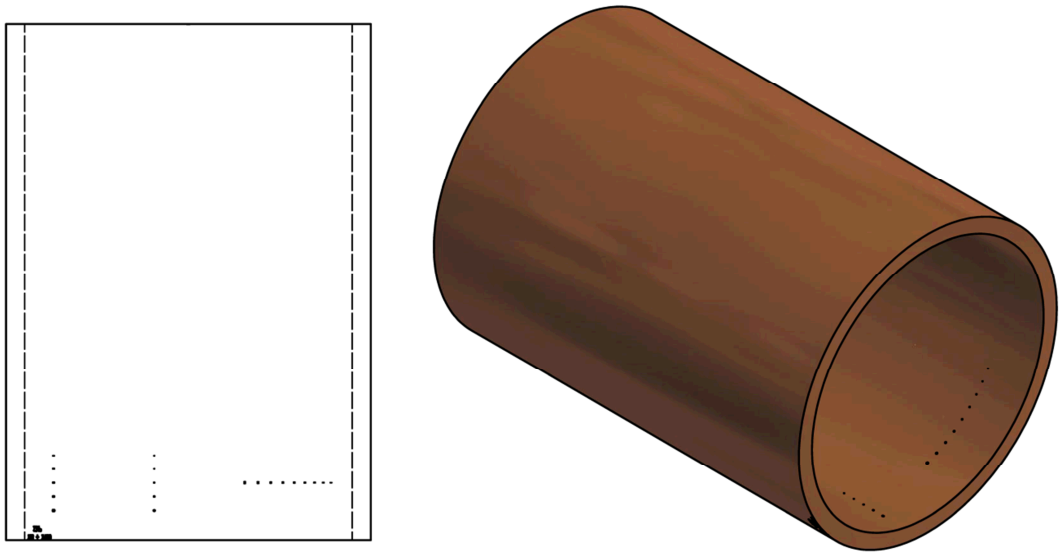

Figure 4-1. *Segment from copper tube T53 with two rows of flat bottom holes in axial direction (high attenuation area) and one row in circumferential direction (low attenuation area).*

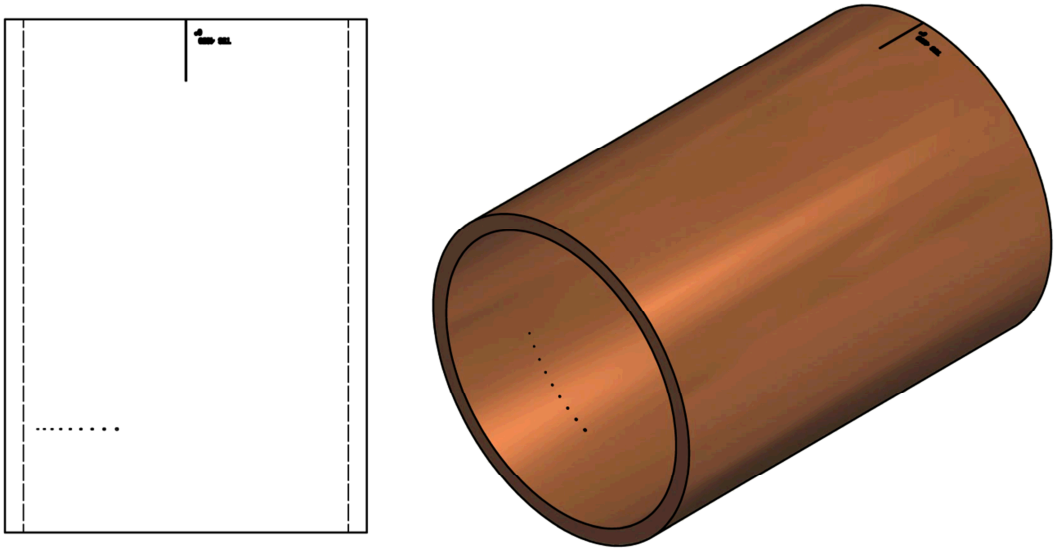

Figure 4-2. *Segment from copper tube T58 with one row of flat bottom holes in circumferential direction.*

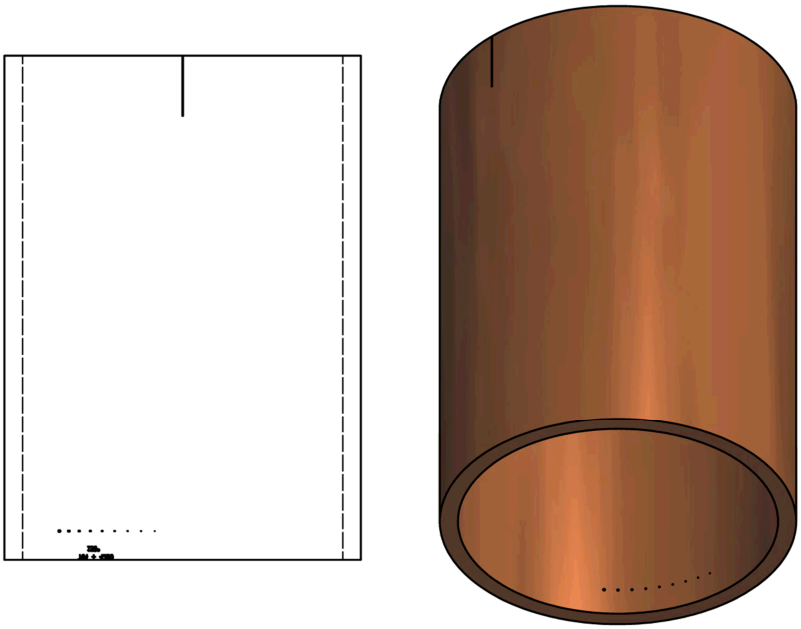

Figure 4-3. *Segment from copper tube T64 with one row of flat bottom holes in circumferential direction.*

From the copper tube segment T53 additional step wedge objects have been manufactured in order to investigate the variations in ultrasonic attenuation along the tube thickness. The step wedge objects (Figure 4-4) have been cut from both the low and the high attenuation areas of this tube. The origin and important sizes can be seen in Table 4-2.

Table 4-2. T53 step wedge objects

Identity	Circ. Pos. (°)	Axial pos (mm)	Plane surface	Thickness step 1 (mm)	Thickness step 2 (mm)	Thickness step 3 (mm)	Attenuation
T53 125/960	125	960	Outer dia.	17	34	49	High
T53 125/1030	125	1030	Inner dia.	17	34	49	High
T53 220/960	220	960	Outer dia.	17	34	49	Low
T53 220/1030	220	1030	Inner dia.	17	34	49	Low

Figure 4-4. *Step wedge objects.*

5 Input Parameters

5.1 Ultrasonic data

For the calculation of the POD-curves, SKB has collected data and delivered to BAM in several steps. All data that is presented here has been collected, see Table 5-1, by the ultrasonic channel "FD40 16elts" as all relevant values are at depth deeper than 20 mm.

5.1.1 Data set 1

The first data set, see Table 5-2 to Table 5-6, included amplitudes from duplicate measurements of all flat bottom holes together with measured amplitudes for corresponding back wall echoes taken in the vicinity of each FBH in the three tube segments (T53, T58 and T64). In Figure 5-1 and Figure 5-2 the principles of the back wall echo measurements in relation to the measurements of the flat bottom holes are shown.

Table 5-1. Collected data files from inspection of the tube segments.

Data file	Date	Table	Data points id.	Measures
T53_0-1485_UT11-2_981-1320	2012-02-15	5-2, 5-3	1-9, 19-27	FBH Amplitude
T53_UT11-2_1182-1295 long gate	2012-12-06	5-2, 5-3	10-18, 28-36	FBH Amplitude
T53_UT11-2_1182-1295 long gate	2012-12-06	5-2, 5-3	1-36	Back wall echo
T58_3530-4850_UT11-2_39-378	2012-02-16	5-4	37-45	FBH Amplitude
T58_UT11-2_3590_long gate	2013-04-25	5-4	46-54	FBH Amplitude
T58_UT11-2_3590_long gate	2012-12-06	5-4	37-54	Back wall echo
T64_2170-4260_UT11-2_3752-4091	2012-02-16	5-5	55-63	FBH Amplitude
T64_UT11-2_4047_long gate	2012-12-06	5-5	64-72	FBH Amplitude
T64_UT11-2_4047_long gate	2012-12-06	5-5	55-72	Back wall echo

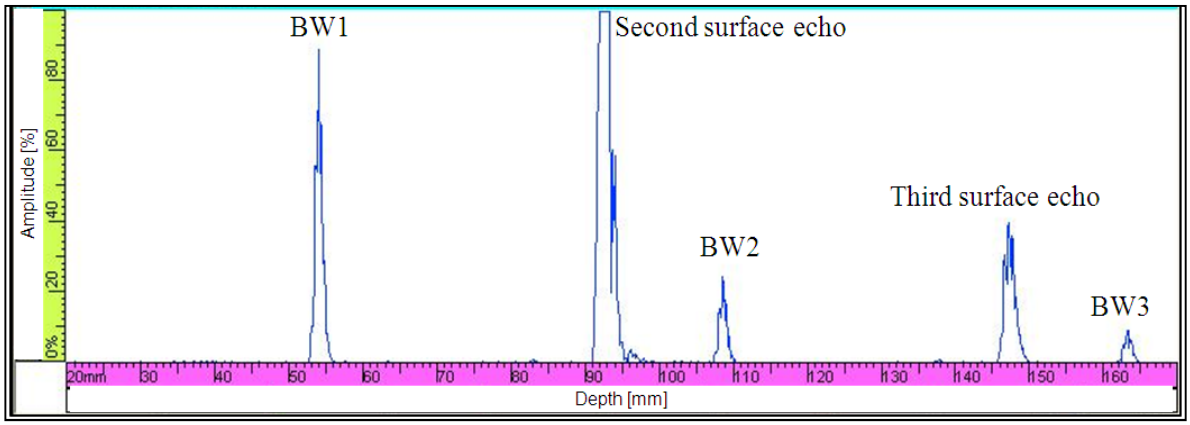

Figure 5-1. *Principle for the measurement of the amplitudes from the multiple back wall (BW) echoes shown in an ultrasonic a-scan.*

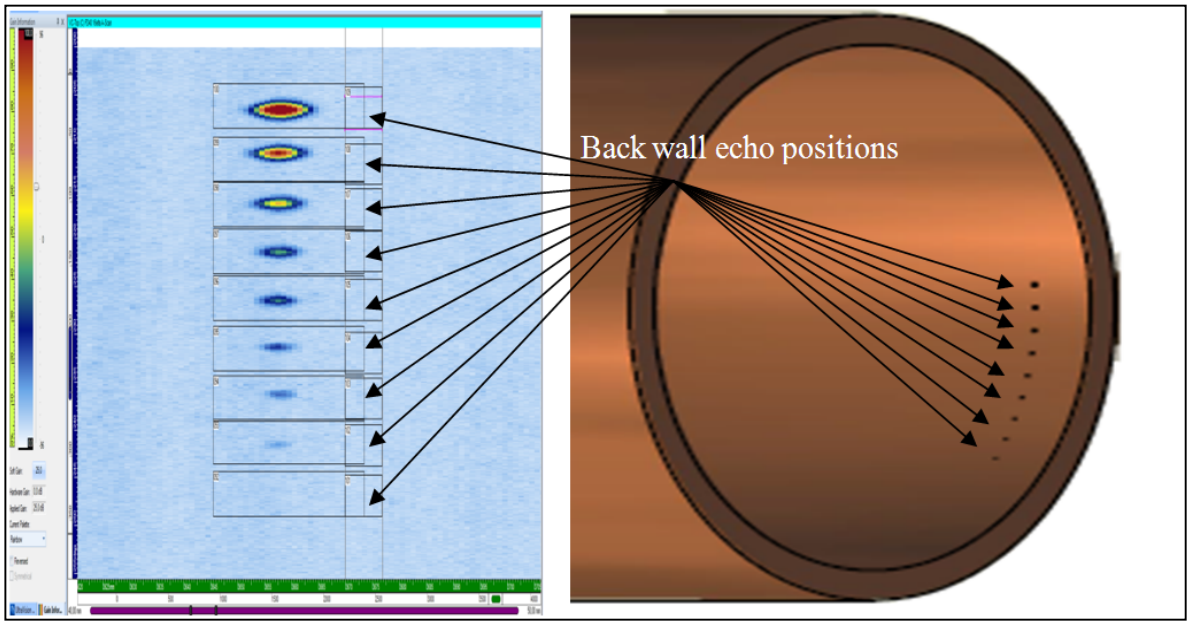

Figure 5-2. *Principle for the measurement of the back wall echo amplitudes in the vicinity of the flat bottom holes. In the left image the c-scan is gated around the depth of the flat bottom holes while the right image shows the model of the T64 tube part.*

Table 5-2. Ultrasonic data for the tube segment T53 low attenuation.

Id.	Noise (%)	Amp (%)	SNR	BW1, 54mm (%)	BW2, 108mm (%)	BW3, 162mm (%)	FBH Ø (mm)	FBH depth (mm)
1	0.37	0.95	2.54	41.54	11.42	4.49	1.0	49.0
2	0.37	2.06	5.54	41.99	11.64	4.60	1.5	49.0
3	0.37	3.33	8.93	42.43	12.09	4.60	2.0	49.0
4	0.37	4.60	12.36	41.99	11.64	4.94	2.5	49.0
5	0.37	5.89	15.81	42.43	12.31	4.60	3.0	49.0
6	0.37	8.65	23.23	46.84	13.43	4.82	3.5	49.0
7	0.37	11.04	29.66	46.37	13.21	5.72	4.0	49.0
8	0.37	14.42	38.73	45.90	12.54	5.39	5.0	49.0
9	0.37	20.55	55.20	41.09	11.87	5.16	6.0	49.0
10	0.28	0.91	3.24	41.54	11.42	4.49	1.0	49.0
11	0.34	2.25	6.66	41.99	11.64	4.60	1.5	49.0
12	0.34	3.45	10.22	42.43	12.09	4.60	2.0	49.0
13	0.34	4.67	13.83	41.99	11.64	4.94	2.5	49.0
14	0.34	6.51	19.29	42.43	12.31	4.60	3.0	49.0
15	0.34	8.07	23.91	46.84	13.43	4.82	3.5	49.0
16	0.34	10.73	31.79	46.37	13.21	5.72	4.0	49.0
17	0.34	14.44	42.80	45.90	12.54	5.39	5.0	49.0
18	0.34	20.06	59.45	41.09	11.87	5.16	6.0	49.0

Table 5-3. Ultrasonic data for the tube segment T53 high attenuation.

Id.	Noise (%)	Amp (%)	SNR	BW1, 54mm (%)	BW2, 108mm (%)	BW3, 162mm (%)	FBH Ø (mm)	FBH depth (mm)
19	0.36	1.09	3.03	10.72	2.02	0.79	2.0	49.0
20	0.40	2.06	5.16	12.51	2.25	0.93	3.0	49.0
21	0.40	1.14	2.85	11.17	1.80	0.78	2.5	49.0
22	0.37	2.87	7.84	12.51	2.25	0.79	4.0	49.0
23	0.37	2.16	5.90	11.17	1.80	0.75	3.5	49.0
24	0.35	5.22	15.05	10.72	2.08	0.81	6.0	49.0
25	0.35	3.51	10.11	10.27	1.63	0.71	5.0	49.0
26	0.37	0.79	2.12	10.27	1.69	0.66	1.5	49.0
27	NA	NA	NA	8.04	1.46	0.61	1.0	49.0
28	0.34	0.88	2.60	10.27	1.69	0.66	1.5	49.0
29	0.34	0.93	2.76	10.72	2.02	0.79	2.0	49.0
30	0.34	1.25	3.70	11.17	1.80	0.78	2.5	49.0
31	0.34	1.86	5.50	12.51	2.25	0.93	3.0	49.0
32	0.34	2.48	7.35	11.17	1.80	0.75	3.5	49.0
33	0.34	2.95	8.73	12.51	2.25	0.79	4.0	49.0
34	0.34	3.72	11.03	10.27	1.63	0.71	5.0	49.0
35	0.34	5.21	15.45	10.72	2.08	0.81	6.0	49.0
36	NA	NA	NA	8.04	1.46	0.61	1.0	49.0

Table 5-4. Ultrasonic data for the tube segment T58 high attenuation.

Id.	Noise (%)	Amp (%)	SNR	BW1, 54mm (%)	BW2, 108mm (%)	BW3, 162mm (%)	FBH Ø (mm)	FBH depth (mm)
37	0.32	9.38	29.66	15.89	3.66	1.47	6.0	49.0
38	0.32	6.18	19.55	14.55	3.26	1.35	5.0	49.0
39	0.32	4.03	12.75	14.10	2.98	1.24	4.0	49.0
40	0.32	2.74	8.65	12.09	2.59	1.13	3.5	49.0
41	0.32	2.31	7.32	11.64	2.47	1.07	3.0	49.0
42	0.32	1.56	4.94	12.09	2.47	1.01	2.5	49.0
43	0.32	1.22	3.87	13.43	2.76	1.18	2.0	49.0
44	0.32	1.04	3.29	14.10	3.21	1.32	1.5	49.0
45	NA	NA	NA	15.89	3.43	1.44	1.0	49.0
46	0.34	0.60	1.77	15.89	3.43	1.44	1.0	49.0
47	0.34	0.87	2.59	14.10	3.21	1.32	1.5	49.0
48	0.34	1.22	3.63	13.43	2.76	1.18	2.0	49.0
49	0.34	1.50	4.44	12.09	2.47	1.01	2.5	49.0
50	0.34	2.31	6.84	11.64	2.47	1.07	3.0	49.0
51	0.34	2.47	7.31	12.09	2.59	1.13	3.5	49.0
52	0.34	3.69	10.93	11.87	2.98	1.24	4.0	49.0
53	0.34	5.73	16.99	12.54	3.26	1.35	5.0	49.0
54	0.34	8.72	25.84	15.89	3.66	1.47	6.0	49.0

Table 5-5. Ultrasonic data for the tube segment T64 high attenuation.

Id.	Noise (%)	Amp (%)	SNR	BW1, 54mm (%)	BW2, 108mm (%)	BW3, 162mm (%)	FBH Ø (mm)	FBH depth (mm)
55	0.32	3.33	10.52	6.58	1.31	0.69	6.0	49.0
56	0.32	1.99	6.29	6.23	1.24	0.62	5.0	49.0
57	0.32	1.44	4.56	6.58	1.35	0.68	4.0	49.0
58	0.32	1.13	3.58	6.30	1.24	0.60	3.5	49.0
59	0.32	0.98	3.10	6.09	1.24	0.66	3.0	49.0
60	0.32	0.79	2.51	6.02	1.35	0.78	2.5	49.0
61	NA	NA	NA	6.23	1.35	0.64	2.0	49.0
62	NA	NA	NA	6.30	1.24	0.64	1.5	49.0
63	NA	NA	NA	6.65	1.35	0.66	1.0	49.0
64	0.34	3.43	10.17	6.58	1.31	0.69	6.0	49.0
65	0.34	2.26	6.69	6.23	1.24	0.62	5.0	49.0
66	0.34	1.66	4.92	6.58	1.35	0.68	4.0	49.0
67	0.34	1.22	3.61	6.30	1.24	0.60	3.5	49.0
68	0.34	1.08	3.20	6.09	1.24	0.66	3.0	49.0
69	0.34	0.95	2.81	6.02	1.35	0.78	2.5	49.0
70	0.34	0.72	2.13	6.23	1.35	0.64	2.0	49.0
71	0.34	0.61	1.80	6.30	1.24	0.64	1.5	49.0
72	NA	NA	NA	6.65	1.35	0.66	1.0	49.0

Table 5-6. Explanation of the headers in Table 5-2 to Table 5-5.

Header	Explanation
Noise (%)	Normalized noise level at 0dB SoftGain
Amp (%)	Normalized FBH amplitude at 0dB SoftGain
SNR	Signal to noise ratio
BW1, 54mm (%)	Normalized amplitude for BW1 at 0dB SoftGain
BW2, 108mm (%)	Normalized amplitude for BW2 at 0dB SoftGain
BW3, 162mm (%)	Normalized amplitude for BW3 at 0dB SoftGain
FBH Ø (mm)	Diameter of flat bottom hole
FBH depth (mm)	Depth of ultrasonic wave path to the FBH

5.1.2 Data set 2

The second data set, see Table 5-7 to Table 5-9, was collected in order to investigate the difference in low-pass filtering due to the difference in material structure in the four different materials. The data points have been collected in the three tube segments (T53, T58 and T64) in the vicinity of each flat bottom hole and the centre frequencies have been extracted by FFT (fast Fourier transform) calculations.

Table 5-7. Collected FFT data files.

Data file	Date	Table	Measures
T53_UT11-2 long gate ch2 FFT 25V puls	2013-04-24	5-8	Surface echo
T53_UT11-2 long gate ch2 FFT 90V puls	2013-04-24	5-8	Back wall echo 1 and 2
T58_UT11-2 long gate ch2 FFT 25V puls	2013-04-25	5-9	Surface echo
T58_UT11-2 long gate ch2 FFT 90V puls	2013-04-25	5-9	Back wall echo 1 and 2
T64_UT11-2 long gate ch2 FFT 25V puls	2013-04-25	5-9	Surface echo
T64_UT11-2 long gate ch2 FFT 90V puls	2013-04-25	5-9	Back wall echo 1 and 2

Table 5-8. Ultrasonic centre frequencies (FFT data) for the tube segment T53.

T53 low attenuation			T53 high attenuation		
Surface echo Frequency (MHz)	Back wall echo 1 Frequency (MHz)	Back wall echo 2 Frequency (MHz)	Surface echo Frequency (MHz)	Back wall echo 1 Frequency (MHz)	Back wall echo 2 Frequency (MHz)
3.17	2.76	2.44	3.15	2.27	1.68
3.17	2.83	2.47	3.13	2.29	1.73
3.17	2.81	2.49	3.15	2.27	1.68
3.17	2.81	2.49	3.13	2.29	1.73
3.17	2.78	2.47	3.17	2.27	1.68
3.17	2.81	2.47	3.17	2.25	1.61
3.17	2.78	2.44	3.10	2.25	1.71
3.17	2.78	2.47	3.13	2.22	1.56
3.17	2.76	2.42	NA	NA	NA

Table 5-9. Ultrasonic centre frequencies (FFT data) for the tube segment T58 and T64.

T58 low attenuation			T64 high attenuation		
Surface echo Frequency (MHz)	Back wall echo 1 Frequency (MHz)	Back wall echo 2 Frequency (MHz)	Surface echo Frequency (MHz)	Back wall echo 1 Frequency (MHz)	Back wall echo 2 Frequency (MHz)
3.20	2.56	2.15	3.20	2.15	1.73
3.20	2.56	2.15	3.20	2.15	1.73
3.20	2.54	2.15	3.20	2.15	1.73
3.20	2.56	2.17	3.20	2.15	1.73
3.17	2.59	2.17	3.20	2.15	1.73
3.17	2.54	2.20	3.20	2.15	1.73
3.20	2.59	2.20	3.20	2.15	1.73
3.20	2.59	2.17	3.20	2.15	1.73
NA	NA	NA	3.20	2.15	1.73

5.1.3 Data set 3

The third data set, see Table 5-10 to Table 5-11, was collected in order to get multiple back wall echoes within the normal inspection depth range down to 55 mm and to examine possible variations along the copper tube thickness. The data was collected on the T53 step wedge test objects by multiple back wall echo reflections according to Figure 5-3 and Figure 5-4.

Table 5-10. Collected data files from inspection of the step wedge objects from tube T53.

Data file	Date	Table	Test object
T53-960-125-UT11_ch2 FFT_long_gate	2013-09-12	5-11	T53-960-125
T53-1030-125-UT11_ch2 FFT_long_gate	2013-09-12	5-11	T53-1030-125
T53-960-220-UT11_ch2 FFT_long_gate	2013-09-12	5-11	T53-960-220
T53-1030-220-UT11_ch2 FFT_long_gate	2013-09-12	5-11	T53-1030-220

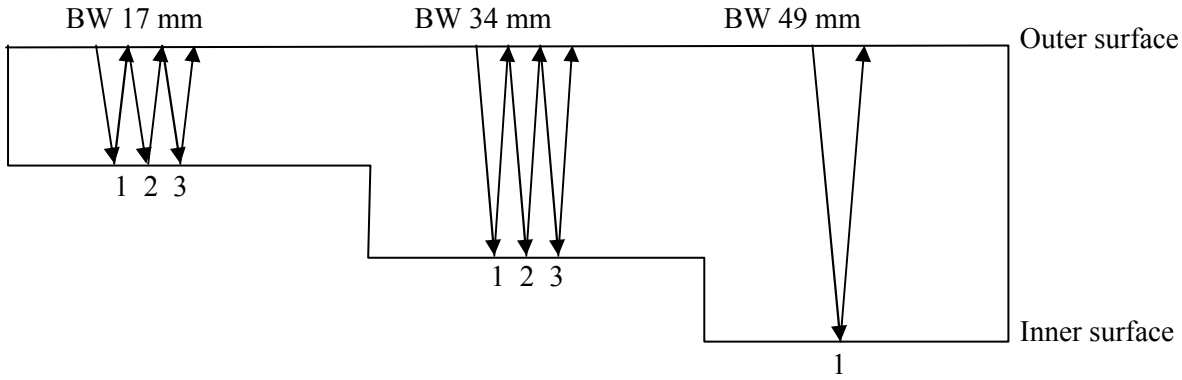

Figure 5-3. *Sketch of the back wall echo positions for test samples T53-960-125 and T53-960-220.*

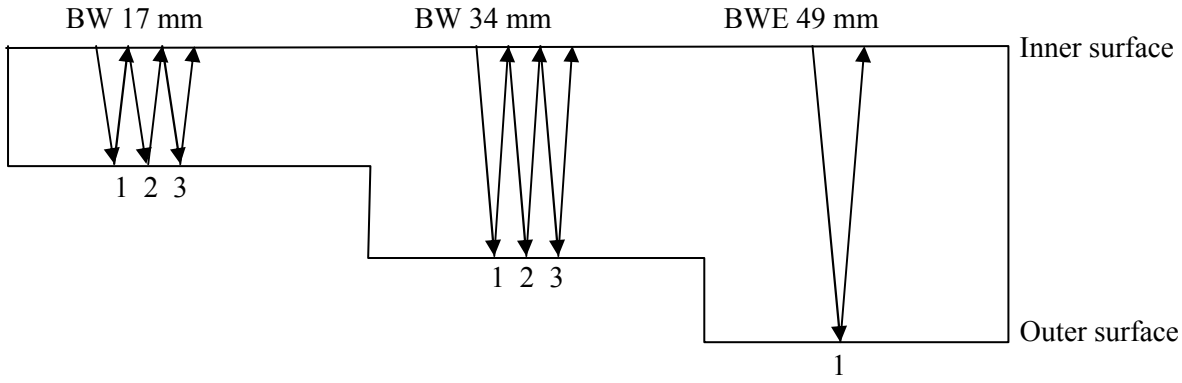

Figure 5-4. *Sketch of the back wall echo positions for test samples T53-1030-125 and T53-1030-220.*

Table 5-11. Ultrasonic data for the step wedge objects from tube T53.

			Back wall echo 1		Back wall echo 2		Back wall echo 3	
Sample	**Inspection surface**	**Thickness (mm)**	**Amp 0dB (%)**	**Centre freq. (MHz)**	**Amp 0dB (%)**	**Centre freq. (MHz)**	**Amp 0dB (%)**	**Centre freq. (MHz)**
T53-960-125	Outer	17	11.73	2.95	12.22	2.93	10.06	2.83
T53-960-125	Outer	34	9.05	2.73	3.37	2.39	1.09	2.12
T53-960-125	Outer	49	5.44	2.47	NA	NA	NA	NA
T53-1030-125	Inner	17	5.95	2.61	3.29	2.42	1.85	2.25
T53-1030-125	Inner	34	6.69	2.59	2.01	2.32	0.89	1.98
T53-1030-125	Inner	49	10.95	2.73	NA	NA	NA	NA
T53-960-220	Outer	17	12,65	3.00	14.17	2.98	11.59	2.91
T53-960-220	Outer	34	15.25	2.95	8.32	2.73	3.52	2.51
T53-960-220	Outer	49	14.84	2.86	NA	NA	NA	NA
T53-1030-220	Inner	17	12.16	2.95	12.94	2.95	10.18	2.83
T53-1030-220	Inner	34	16.01	3.03	8.87	2.81	2.95	2.66
T53-1030-220	Inner	49	16.70	2.93	NA	NA	NA	NA

5.2 Modelling data

The modelling calculations were carried out at BAM using the "Array2D3D 6.0DynV3" software for the calculation of the sound field and the "Echo3D 17V3". The physical background and the numerical method are described by Boehm et al. (2009). The sound pressure was calculated along the sound field not directly on the centre axis but at the position of the maximum at the depth of 49 mm. The back wall echo (BWE) was calculated for the depth of 54 mm. The attenuation was not yet included in this calculation. It will be included stepwise in the calculations described in chapter 6. The data are listed in Table 5-12 to Table 5-14.

Table 5-12. Input parameters for modelling of UT11

Probe	**Frequency (MHz)**	**Focal distance (mm)**	**Number of elements**	**Incidence angle (°)**	**Water path (mm)**
SKB 3.5 MHz	3.5	40	16	0	30

Table 5-13. Modelled ultrasonic data for UT11 (without attenuation)

FBH (mm)	0.5	1.0	1.5	2.0	2.5	3.0	3.5	4.0	4.5	5.0	5.5	6.0
Amp (dB)	5.43	6.43	13.28	18.09	21.63	24.42	26.72	28.56	30.07	31.33	32.37	33.28
Back Wall Echo at 54 mm depth (dB)					39.14							
Back Wall Echo at 108mm depth					34.66							

Table 5-14. Back wall echoes (incl. beam spreading) for the T53 step wedge

Depth [mm]	**Calc. BWE [dB]**	**Calc. BWE [%]**
17	36.73	50.86
34	40.20	76.18
49	39.69	71.53
51	39.57	70.55
68	38.13	59.77

6 Multi-Parameter POD

6.1 Multi-parameter analyses

In a former project phase it was discovered that the material attenuation in copper can vary considerably in materials used for the production of the canister components. The change in material attenuation in thick components is recognized as an important influencing factor on the POD. Therefore, the coefficient of material attenuation has to be included as a parameter in the multi-parameter analysis and the POD curve needs to be calculated and expressed as its function (Pavlovic et al. 2010).

In this former research phase the attenuation coefficient α was determined as a function of the x-y (surface) position on the copper part. This approach has shown to be sufficient for the copper material with homogeneous attenuating properties. In the case of the copper tube components, the grain size distributions, which occur as a consequence of the manufacturing process, yield not only high and heterogeneous attenuation coefficients but they also create a low pass filtering on the ultrasonic frequency spectrum. This can be seen in Figure 6-1 through the decrease of the attenuation coefficient determined from the first and the second and from the second and the third back wall echo. The attenuation coefficient, determined from the second and the third back wall echo, is only a third in magnitude with respect to the one determined from the first and the second BWE.

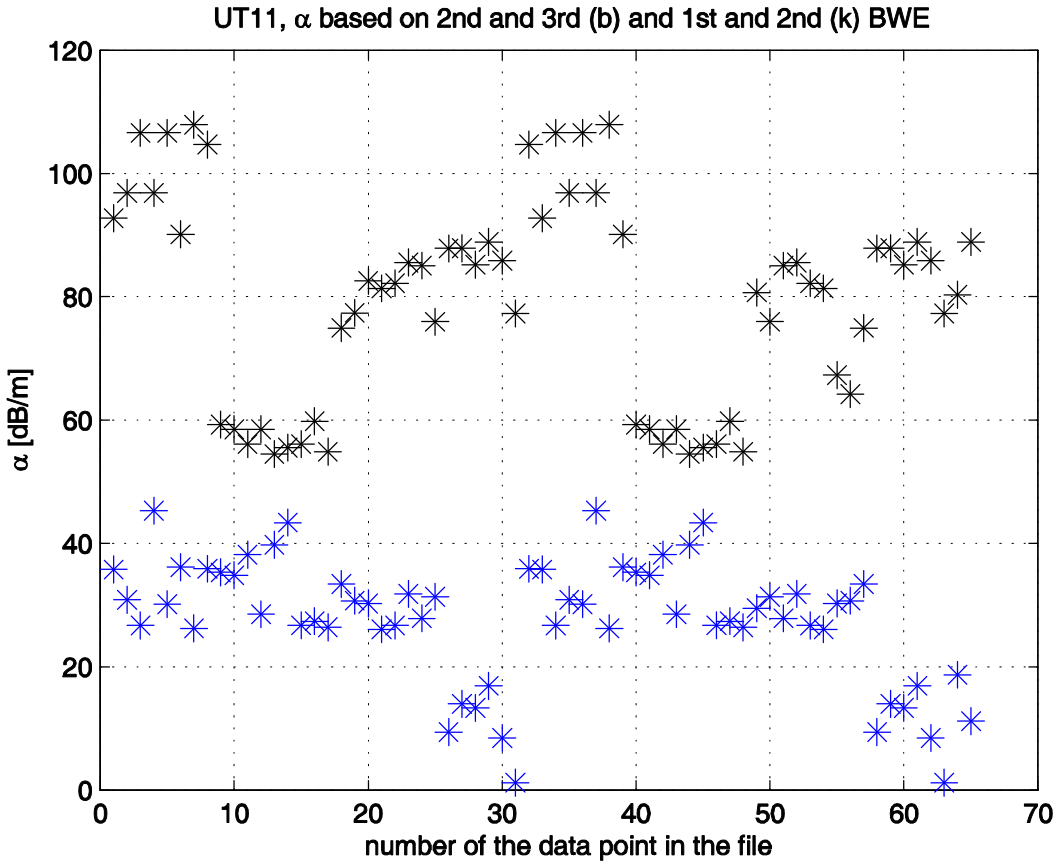

Figure 6-1. *Attenuation coefficient determined from the first and the second (black) and from the second and the third (blue) back wall echo, where the geometrical beam spreading and the transition loss between copper and water is considered (subtracted). The measured back wall echoes were taken from the Tables 5-2 to 5-5.*

The hypothesis that this is caused by filtering out the higher frequencies is confirmed by the FFT analysis as presented in Table 5-8 and Table 5-9. Figure 6-2 shows qualitatively the behaviour of decreasing sound amplitude, centre frequency and attenuation coefficient α as a function of the ultrasonic travel path in copper tube material with heterogeneous grain size distribution (*BWEi* denotes the corresponding travel distance belonging to the i-th back wall echo and *SEi* the travel distance in copper belonging to the i-th surface echo). From this figure it is seen that taking the difference (dB) between the first and the second BWE gives only a first assessment of α (called α_0 below). This first assessment does not consider the low pass filtering from the surface to the defect position or to the first back wall echo. This means that the actual α in the region from the surface to the defect is higher. From the measurements and FTT analysis in the tables 5-8 to 5-9 the frequency shift is compiled in Table 6-1. Whereas the centre frequency for T53low is only decreased by 12%, the decrease for the most attenuating tube T64high is as high as 34%.

As described in chapter 2 and by Pavlovic et al. (2010), the multi-parameter $\hat{a}$ versus a approach consists of considering the measured signal $\hat{a}$ as a function of the multi-parameter a, which, in an optimal way, contains all the influencing parameters. The optimal way is realized in terms of the modelled echo amplitude, as described in chapter 2.

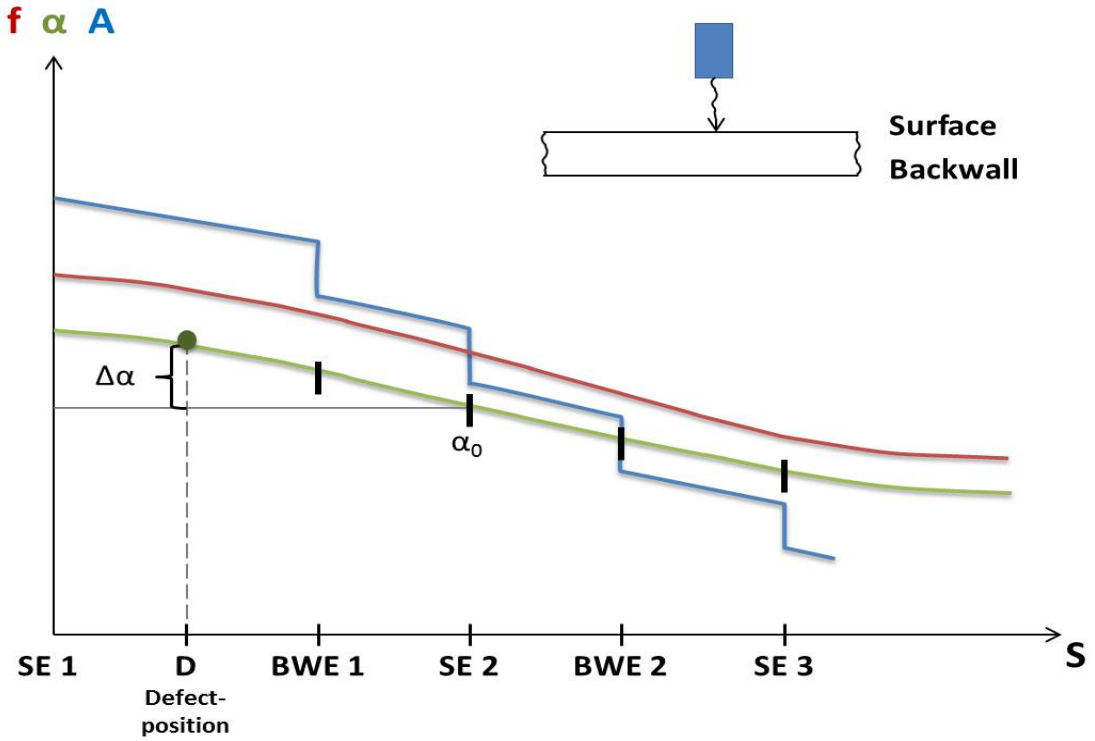

Figure 6-2. *Attenuation coefficient and mid-frequency and amplitude postulated as a function of the UT wave travel distance (S) with SE1 denoting the position of the first surface echo; D - the position of the defect or FBH in the material; BWE1- the position of the first back wall echo; SE2 - the position of the second surface echo, etc. The blue curve represents the UT-Amplitude, the red curve the centre frequency and the green the actual material attenuation coefficient. α_0 represents the first iteration of the attenuation coefficient from the first and the second BWE ratio positioned between them. $\Delta\alpha$ denotes the difference between α_0 and the actual value in the defect region*

Table 6-1. Frequency shift from the surface echo to the first back wall echo.

Tube Segment	Centre frequency, surface echo (MHz)	Centre frequency, 1st BWE (MHz)	Delta centre frequency (MHz)	Delta centre frequency (%)
T53 low	3.2	2.8	0.4	12
T58 high	3.2	2.6	0.6	19
T53 high	3.2	2.3	0.9	28
T64 high	3.2	2.1	1.1	34

The following step is to determine the actual local α. The correct α shall be used to complete the modelling correctly for each attenuation range. Since the attenuation is relatively simply described by an exponential factor all measured data can be renormalized to "α cleaned values "– as if there would be no attenuation at all. These values can be used for an $\hat{a}$ versus a diagram, showing the modelled amplitude without attenuation on the X-axis. The motivation for this re-normalization is to use the α *cleaned* values as a basis for the creation of the PODs for different levels of α with a good statistical basis. The detailed steps of the determination of the actual local α and the multi-parameter $\hat{a}$ versus a are described in detail in Appendix 1. In this section the focus is on the understanding of the flow of physical relations and the references to the corresponding columns in Table 6-2 to Table 6-5.

For the purposes of the multi-parameter POD analysis the measured amplitudes from the flat bottom holes with various diameters, ranging from 1 to 6 mm, from the tube segments T53low, T53high, T58high and T64high at the depth of 49 mm were taken as the $\hat{a}$ (Tables 5-2 to Table 5-5; third column). These values are plotted in Figure 6-3 together with the modelled amplitudes. When there is no measured value available (defect not detected) then the values are determined to be positioned at the maximum noise level resulting in the column *Censored Amp* (step one), which Berens (1989) denotes as "censoring". This is important because the sizes of the defects, which were not found, are essential for the formation of the POD curve. The next step consists of calibrating the modelled amplitude to the experiment, assuming $\Delta\alpha=0$ for T53 low. This calibration is done using a least square fit between model and T53 measurement values with respect to the model factor (MF). The result is shown in figure 6-5.

The aim of the next steps is to determine the multi-parameter â versus a diagram. In the former investigation conducted by Pavlovic et al. (2010), the modelled amplitudes were calibrated by the appropriate attenuation factor to receive a correct assignment of the measured $\hat{a}$*'s* (column 2 and 8) to the modelled *a's* (column 10). We follow this approach to determine the remaining $\Delta\alpha$ in Appendix 1. In order to determine α *cleaned* data, we selected the other way around to calibrate the measured values $\hat{a}$ by the correct attenuation factor until they correspond to the ideal curve for the modelled amplitude (45° line) without attenuation. Because the underlying physical-mathematical relation is the same, the physics is not changed.

$$\hat{a} = MF \cdot e^{-\alpha \cdot S} \cdot a \qquad \text{Formula 6-1}$$

where $\hat{a}$ is the censored measured amplitude (column 8), *MF* the factor to calibrate the modelled data to the experiment in general, α is the correct actual attenuation coefficient, *S* is the sound path (2 times the depth) and *a* is the modelled amplitude at the depth without the attenuation included (column 10).

The following step is to create a correct calibration of the measured values, referred to as "α cleaned" , to the 45° curve by dividing them by $MF \cdot e^{-\alpha \cdot S}$, where the measured amplitude grows in the same way as the modelled amplitude. The advantage of the resulting α *cleaned* data set is that it provides to include all the results from the different tube segments as a serious statistical basis to be available for the multi parameter POD in a correct way. Furthermore, the data set can be used for being re-calibrated again to different possible α values, which might occur in the copper tubes, as long as the exponential attenuation law is valid.

The problem in carrying out the correct calibration of *α cleaned* values is simply the knowledge of the correct *α* in the region between the surface and the defect. We assume – as explained in the context of figure 6-2 - the *α* in formula 6-1 is composed of $\alpha_0 + \Delta\alpha$.

In the next step, a first assessment of the attenuation coefficient α_0 in the neighbourhood of the FBH's is done, following the approach developed by Pavlovic et al. (2010). According to his approach, the material attenuation is determined by the difference of the back wall echoes corrected by the transmission loss from copper to water and the beam spreading loss due to the geometry of the sound field. This is done by taking the BWE values from Table 5-2 to Table 5-5, transforming them into dB and then re-calculating them into dB/m.

$$\alpha_i = \frac{BWE1_i[dB] - BWE2_i[dB]}{2 \cdot depth_i} \cdot 1000 \text{ (equal to step two)} \qquad \text{Formula 6-2}$$

The index i stands for the location of the corresponding FBH in the selected tube section (T53 low, etc.). The next step includes the corrections from beam spreading (modelled BWEs from table 5-14)

$$\alpha_i = \frac{BWE1_i[dB] - BWE2_i[dB] + VT + SK_i}{2 \cdot depth_i} \cdot 1000 \text{ corresponds to } \alpha 0 \text{ (step three)} \qquad \text{Formula 6-3}$$

where VT is the transition loss difference from copper to water between the second and the first BWE of about 0.75 and *SKi* is the difference in beam spreading correction between the first and the second BWE. The value in dB/m is presented in the column 7, α from BW2-BW1 [dB/m], of the Tables 6-2 to Table 6-5 which corresponds to results according to the formula 6-3.

Table 6-2. Input and stepwise evaluated data, T53low.

ID	Amp 0dB (%)	FBH Ø (mm)	BW1 abs. [dB]	BW2 abs. [dB]	BW2-BW1 [dB]	α from BW2-BW1 [dB/m] α_0	Censored Amp [%]	Censored Amp (incl. α normalization, model factor, α, Δα) [%]	a modelled [%]	Δα [dB/m]	α+ Δα [dB/m]
1	0.95	1.0	-7.6	-18.8	-11.2	41.3	0.95	2.36	2.10	0	41.3
2	2.06	1.5	-7.5	-18.7	-11.1	40.6	2.06	5.10	4.61	0	40.6
3	3.33	2.0	-7.4	-18.4	-10.9	38.4	3.33	8.03	8.03	0	38.4
4	4.60	2.5	-7.5	-18.7	-11.1	40.6	4.60	11.38	12.23	0	40.6
5	5.89	3.0	-7.4	-18.2	-10.7	36.9	5.89	13.98	16.81	0	36.9
6	8.65	3.5	-6.6	-17.4	-10.8	37.9	8.65	20.76	21.65	0	37.9
7	11.04	4.0	-6.7	-17.6	-10.9	38.4	11.04	26.66	26.79	0	38.4
8	14.42	5.0	-6.8	-18.0	-11.3	41.8	14.42	36.16	36.90	0	41.8
9	20.55	6.0	-7.7	-18.5	-10.8	37.3	20.55	49.01	46.29	0	37.3
10	0.91	1.0	-7.6	-18.8	-11.2	41.3	0.91	2.27	2.10	0	41.3
11	2.25	1.5	-7.5	-18.7	-11.1	40.6	2.25	5.56	4.61	0	40.6
12	3.45	2.0	-7.4	-18.4	-10.9	38.4	3.45	8.32	8.03	0	38.4
13	4.67	2.5	-7.5	-18.7	-11.1	40.6	4.67	11.55	12.23	0	40.6
14	6.51	3.0	-7.4	-18.2	-10.7	36.9	6.51	15.45	16.81	0	36.9
15	8.07	3.5	-6.6	-17.4	-10.8	37.9	8.07	19.36	21.65	0	37.9
16	10.73	4.0	-6.7	-17.6	-10.9	38.4	10.73	25.90	26.79	0	38.4
17	14.44	5.0	-6.8	-18.0	-11.3	41.8	14.44	36.22	36.90	0	41.8
18	20.06	6.0	-7.7	-18.5	-10.8	37.3	20.06	47.84	46.29	0	37.3

Table 6-3. Input and stepwise evaluated data, T53high.

ID	Amp 0dB (%)	FBH Ø (mm)	BW1 abs. [dB]	BW2 abs. [dB]	BW2-BW1 [dB]	α from BW2-BW1 [dB/m] α_0	Censored Amp [%]	Censored Amp (incl. α normalization, model factor, α, Δα) [%]	a modelled [%]	Δα [dB/m]	α+ Δα [dB/m]
19	1.09	2.0	-19.4	-33.9	-14.5	71.5	1.09	8.26	8.03	68	139.5
20	2.06	3.0	-18.1	-33.0	-14.9	75.4	2.06	16.27	16.81	68	143.4
21	1.14	2.5	-19.0	-34.9	-15.9	84.2	1.14	9.93	12.23	68	152.2
22	2.87	4.0	-18.1	-33.0	-14.9	75.4	2.87	22.76	26.79	68	143.4
23	2.16	3.5	-19.0	-34.9	-15.9	84.2	2.16	18.92	21.65	68	152.2
24	5.22	6.0	-19.4	-33.6	-14.2	69.3	5.22	38.60	46.29	68	137.3
25	3.51	5.0	-19.8	-35.8	-16.0	85.4	3.51	31.10	36.90	68	153.4
26	0.79	1.5	-19.8	-35.5	-15.7	82.7	0.79	6.78	4.61	68	150.7
27	NA	1.0	-21.9	-36.7	-14.8	74.5	0.40	3.12	2.10	68	142.5
28	0.88	1.5	-19.8	-35.5	-15.7	82.7	0.88	7.54	4.61	68	150.7
29	0.93	2.0	-19.4	-33.9	-14.5	71.5	0.93	7.04	8.03	68	139.5
30	1.25	2.5	-19.0	-34.9	-15.9	84.2	1.25	10.92	12.23	68	152.2
31	1.86	3.0	-18.1	-33.0	-14.9	75.4	1.86	14.70	16.81	68	143.4
32	2.48	3.5	-19.0	-34.9	-15.9	84.2	2.48	21.69	21.65	68	152.2
33	2.95	4.0	-18.1	-33.0	-14.9	75.4	2.95	23.33	26.79	68	143.4
34	3.72	5.0	-19.8	-35.8	-16.0	85.4	3.72	33.01	36.90	68	153.4
35	5.21	6.0	-19.4	-33.6	-14.2	69.3	5.21	38.51	46.29	68	137.3
36	NA	1.0	-21.9	-36.7	-14.8	74.5	0.40	3.12	2.10	68	142.5

Table 6-4. Input and stepwise evaluated data, T58high.

ID	Amp 0dB (%)	FBH Ø (mm)	BW1 abs. [dB]	BW2 abs. [dB]	BW2-BW1 [dB]	α from BW2-BW1 [dB/m] α_0	Censored Amp [%]	Censored Amp (incl. α normalization, model factor, α, Δα) [%]	a modelled [%]	Δα [dB/m]	α+ Δα [dB/m]
37	9.38	6.0	-16.0	-28.7	-12.8	55.6	9.38	56.27	46.29	63	118.6
38	6.18	5.0	-16.7	-29.7	-13.0	57.7	6.18	37.96	36.90	63	120.7
39	4.03	4.0	-17.0	-30.5	-13.5	62.4	4.03	26.12	26.79	63	125.4
40	2.74	3.5	-18.4	-31.7	-13.4	61.4	2.74	17.52	21.65	63	124.4
41	2.31	3.0	-18.7	-32.1	-13.5	62.0	2.31	14.92	16.81	63	125.0
42	1.56	2.5	-18.4	-32.1	-13.8	65.0	1.56	10.42	12.23	63	128.0
43	1.22	2.0	-17.4	-31.2	-13.8	64.8	1.22	8.14	8.03	63	127.8
44	1.04	1.5	-17.0	-29.9	-12.9	56.6	1.04	6.31	4.61	63	119.6
45	NA	1.0	-16.0	-29.3	-13.3	60.7	0.40	2.53	2.10	63	123.7
46	0.60	1.0	-16.0	-29.3	-13.3	60.7	0.60	3.80	2.10	63	123.7
47	0.87	1.5	-17.0	-29.9	-12.9	56.6	0.87	5.30	4.61	63	119.6
48	1.22	2.0	-17.4	-31.2	-13.8	64.8	1.22	8.14	8.03	63	127.8
49	1.50	2.5	-18.4	-32.1	-13.8	65.0	1.50	10.00	12.23	63	128.0
50	2.31	3.0	-18.7	-32.1	-13.5	62.0	2.31	14.88	16.81	63	125.0
51	2.47	3.5	-18.4	-31.7	-13.4	61.4	2.47	15.80	21.65	63	124.4
52	3.69	4.0	-18.5	-30.5	-12.0	48.5	3.69	20.43	26.79	63	111.5
53	5.73	5.0	-18.0	-29.7	-11.7	45.7	5.73	30.76	36.90	63	108.7
54	8.72	6.0	-16.0	-28.7	-12.8	55.6	8.72	52.31	46.29	63	118.6

Table 6-5. Input and stepwise evaluated data, T64high.

ID	Amp 0dB (%)	FBH Ø (mm)	BW1 abs. [dB]	BW2 abs. [dB]	BW2-BW1 [dB]	α from BW2-BW1 [dB/m] α_0	Censored Amp [%]	Censored Amp (incl. α normalization, model factor, α, Δα) [%]	a modelled [%]	Δα [dB/m]	α+ Δα [dB/m]
55	3.33	6.0	-23.6	-37.6	-14.0	67.1	3.33	45.30	46.29	125	192.1
56	1.99	5.0	-24.1	-38.1	-14.0	67.1	1.99	27.11	36.90	125	192.1
57	1.44	4.0	-23.6	-37.4	-13.8	64.9	1.44	19.18	26.79	125	189.9
58	1.13	3.5	-24.0	-38.1	-14.1	68.0	1.13	15.59	21.65	125	193.0
59	0.98	3.0	-24.3	-38.1	-13.8	65.3	0.98	13.07	16.81	125	190.3
60	0.79	2.5	-24.4	-37.4	-13.0	57.7	0.79	9.73	12.23	125	182.7
61	NA	2.0	-24.1	-37.4	-13.3	60.5	0.40	5.04	8.03	125	185.5
62	NA	1.5	-24.0	-38.1	-14.1	68.0	0.40	5.49	4.61	125	193.0
63	NA	1.0	-23.5	-37.4	-13.9	65.8	0.40	5.35	2.10	125	190.8
64	3.43	6.0	-23.6	-37.6	-14.0	67.1	3.43	46.74	46.29	125	192.1
65	2.26	5.0	-24.1	-38.1	-14.0	67.1	2.26	30.75	36.90	125	192.1
66	1.66	4.0	-23.6	-37.4	-13.8	64.9	1.66	22.08	26.79	125	189.9
67	1.22	3.5	-24.0	-38.1	-14.1	68.0	1.22	16.76	21.65	125	193.0
68	1.08	3.0	-24.3	-38.1	-13.8	65.3	1.08	14.40	16.81	125	190.3
69	0.95	2.5	-24.4	-37.4	-13.0	57.7	0.95	11.61	12.23	125	182.7
70	0.72	2.0	-24.1	-37.4	-13.3	60.5	0.72	9.11	8.03	125	185.5
71	0.61	1.5	-24.0	-38.1	-14.1	68.0	0.61	8.35	4.61	125	193.0
72	NA	1.0	-23.5	-37.4	-13.9	65.8	0.40	5.35	2.10	125	190.8

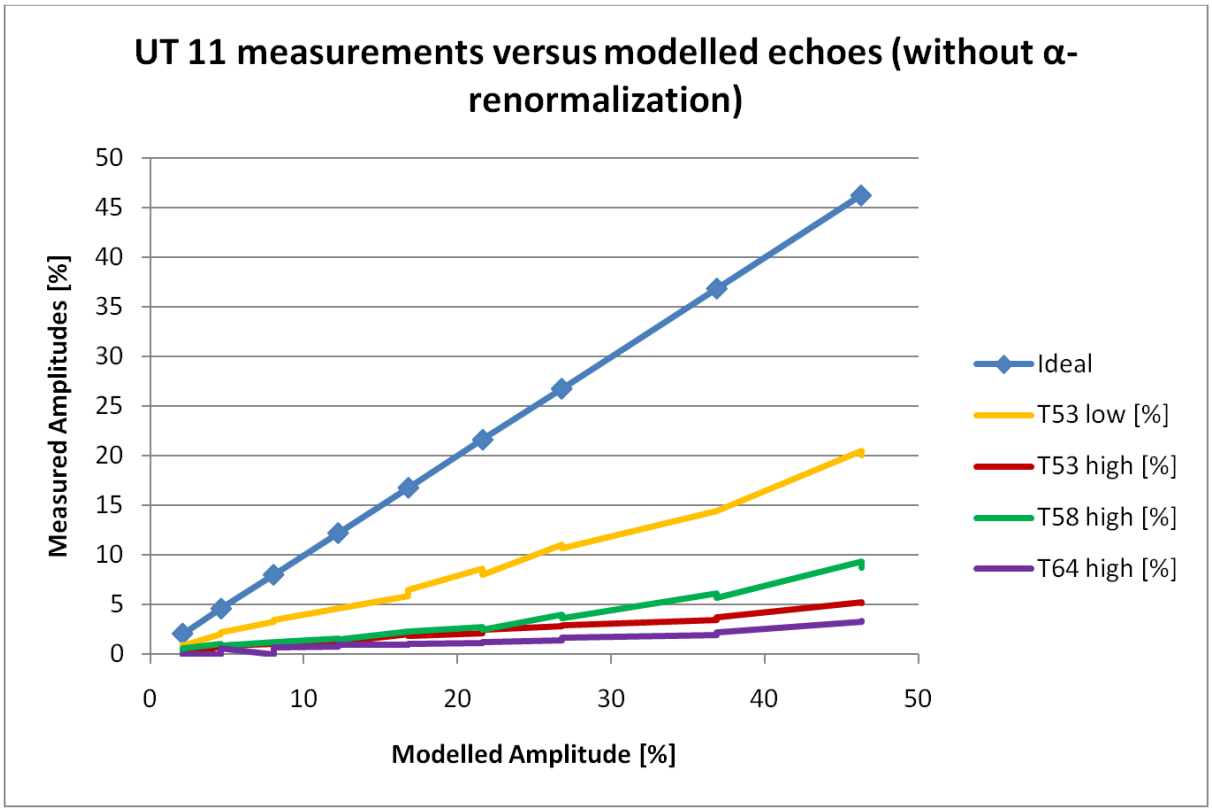

Figure 6-3. *Measured amplitudes (Y-axis) plotted as a function of the not yet calibrated modelled amplitude (X-axis).*

It is well seen in Figure 6-3 that the amplitudes from the same depth and the same FBH diameter are different due to the different attenuation in the material. As a next step, as described above, the attenuation coefficients were calculated on the basis of the difference between the first and the second BWE, beam spreading correction and transmission losses (Cu-water), as indicated for each FBH surrounding and attenuation quality of the tube part in Figure 6-6 and as described in steps 1-3 above.

In order to create a multi-parameter $\hat{a}$ versus a-diagram, an a including the attenuation could be created, as done by Pavlovic et al. (2010). However, it was decided to re-normalize the measured values by the attenuation factor in order to create a multi-parameter data set with the attenuation excluded. This allows us to include any α of interest and make forecasts for the POD for a minimum, medium and maximum α.

Following this logic, the measured amplitudes were renormalized by the factor exp(- $\alpha_0 \cdot S$), where α_0 is the attenuation coefficient determined from the BWE differences, beam spreading and transition losses and S is the ultrasound-travel distance (two times depth, in our case). The result is shown in Figure 6-4 while the first iteration of α renormalized measurements and the α_0 results are shown in Figure 6-7.

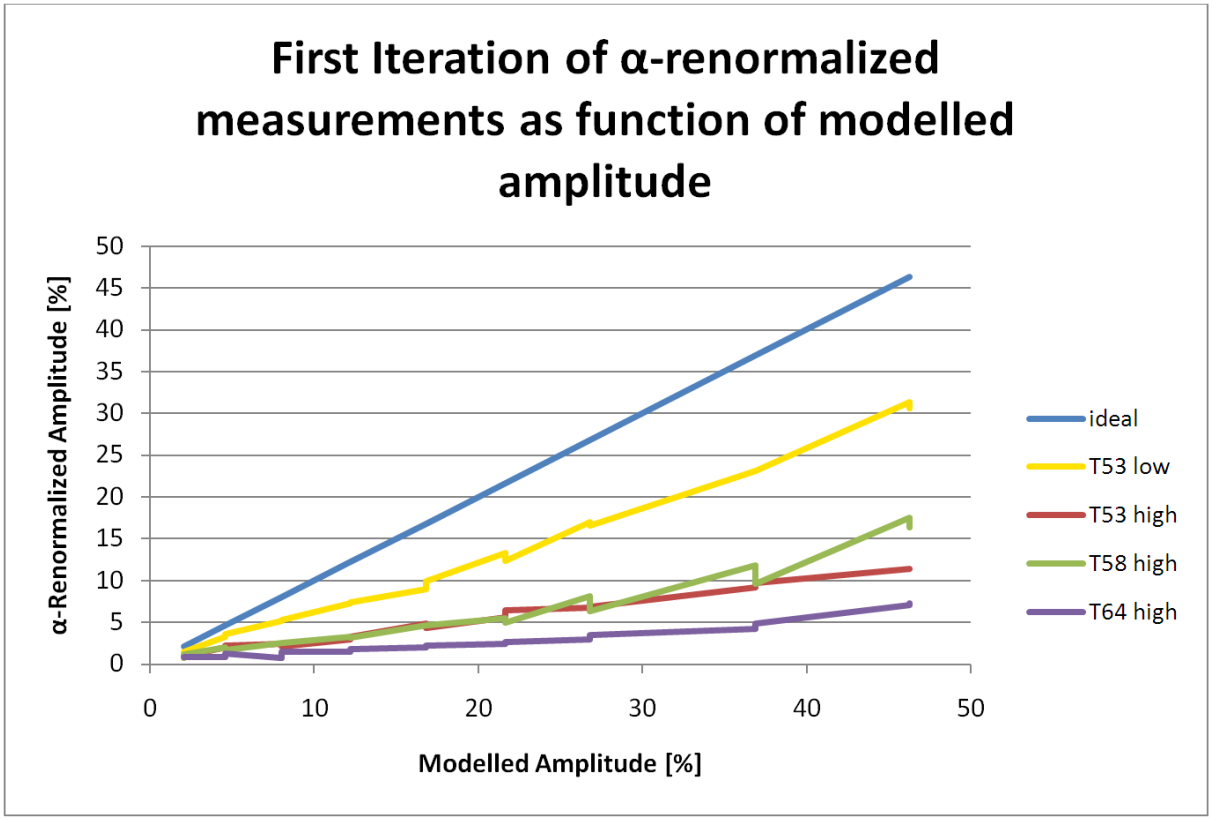

Figure 6-4. *First iteration of* α*-renormalized measurements as function of modelled amplitude.*

When the curves for the different materials are compared to the ideal curve, it can be seen that the curves for higher attenuating material differ more from the linear behaviour, especially for higher amplitudes (corresponding to larger FBH diameters, as seen in Figure 6-9). That means that the measured amplitudes grow faster with the diameter than the modelled one. This phenomenon will be discussed in sub-chapter 6.2 in the context of the frequency shift.

The question arose how the $\Delta\alpha$, i.e. the difference of α taken from the BWEs with respect to the actual value between the surface and the FBH, could be determined without too high experimental effort.

The $\Delta\alpha$ is caused by the low pass filtering behaviour, as well as by the heterogeneity of grain size distribution in depth-direction. Figure 6-4 with the preliminary (by α from first and second BWE) renormalized measurements shows that T53low does deviate only slightly from the ideal curve. Based on the shifts of centre frequencies from the surface echo and the first BWE on the basis of Table 6-1 we defined the $\Delta\alpha$ to be zero for T53low. In Figure 6-5 together with calibrated model (factor MF) – we see that for higher attenuation the differences are still high.

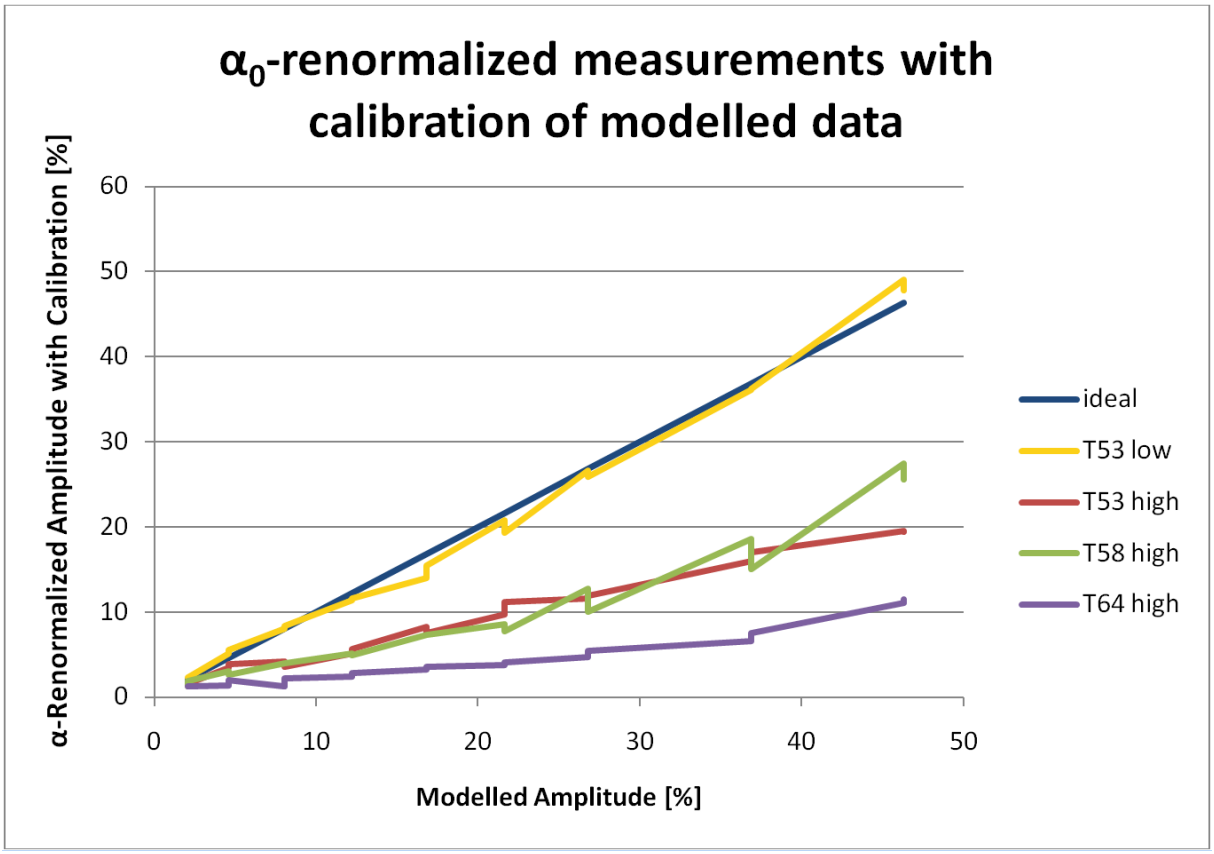

Figure 6-5. α *renormalized measurements with calibration of modelled data.*

If our model describes the underlying physics correctly, i.e. including attenuation, then the renormalized curves should all follow the ideal (= modelled curve) besides the individual scatter. However, this is not the case since we know about the low pass filtering shift. What we can do is to determine the $\Delta\alpha$ by fitting the correctly modelled curves using the factor $exp(-\Delta\alpha)$ to each set of experimental data, as explained in Appendix 1. The resulting $\Delta\alpha$ values are shown in the Appendix 1 and equal 60 dB/m for T53high, 63 dB/m for T58 high and 125 dB/m for T64high. Furthermore, it might be necessary to adapt the underlying modelling of a for higher attenuation to the actual frequency range, as mentioned in the argumentation above and in subchapter 6.2. The results after the $\Delta\alpha$ shift are shown in Figure 6-6.

All α-renormalized curves follow the ideal curve. This α free data set represents the basic data from which the extrapolation to any α values can be carried out. The determined $\Delta\alpha$ are indicated in the diagrams in Appendix 1 and also listed above (column 11 in Table 6-2 Table to 6-5). The final α values are shown in Figure 6-8 indicated for each FBH surrounding and listed in Table 6-2 to Table 6-5 (column 12). As it should be, according to the measurement values, the final α follow the order T53low, T58high, T53high and T64high. For T53high, the difference in attenuation for the two axial FBH rows is well reflected by the zigzag line.

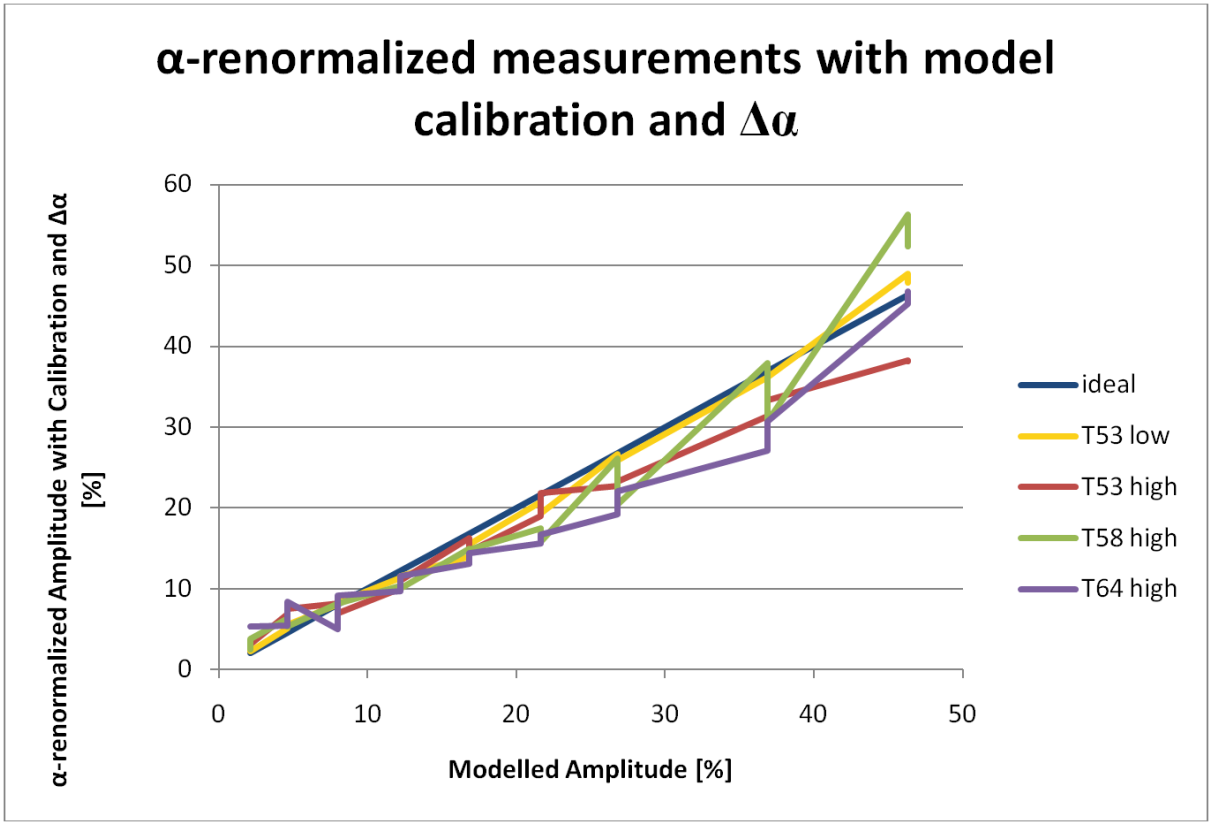

Figure 6-6. *α-renormalized measurements with model calibration and Δα.*

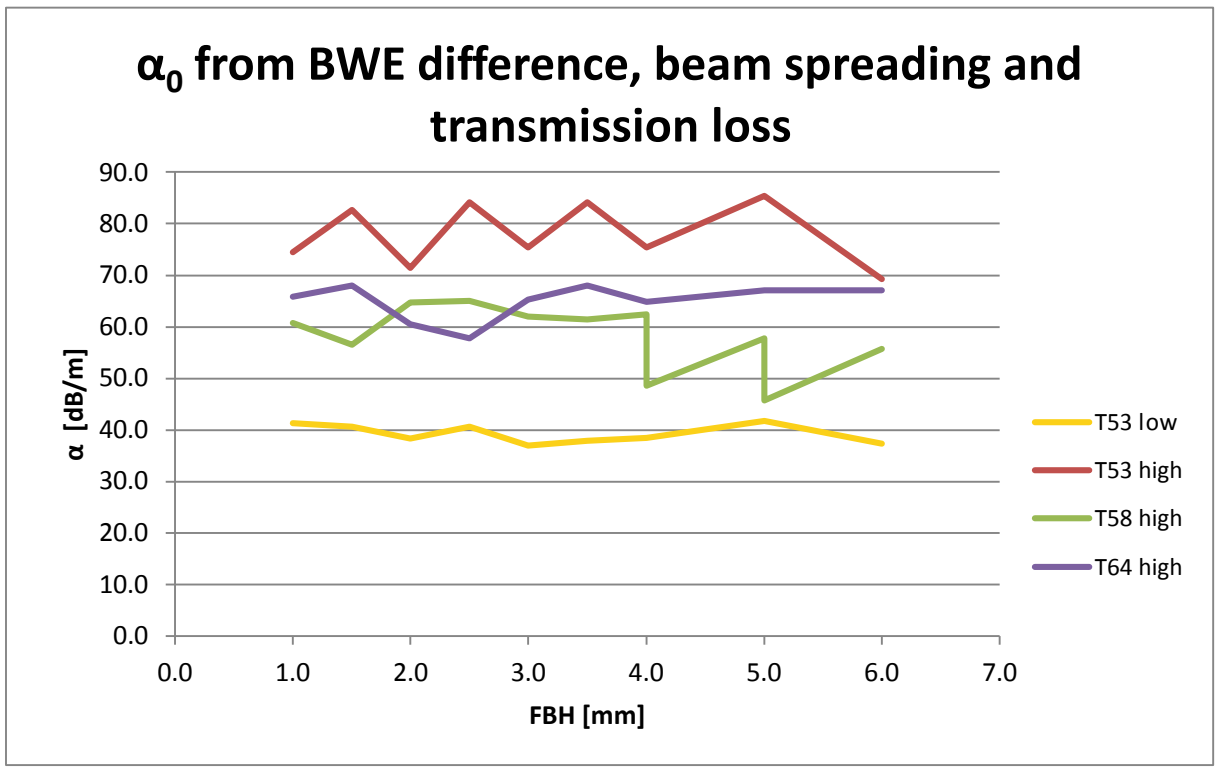

Figure 6-7. *Attenuation coefficients calculated on the basis of the difference between the first and the second BWE, beam spreading correction and transmission losses (Cu-water), as indicated for each FBH surrounding.*

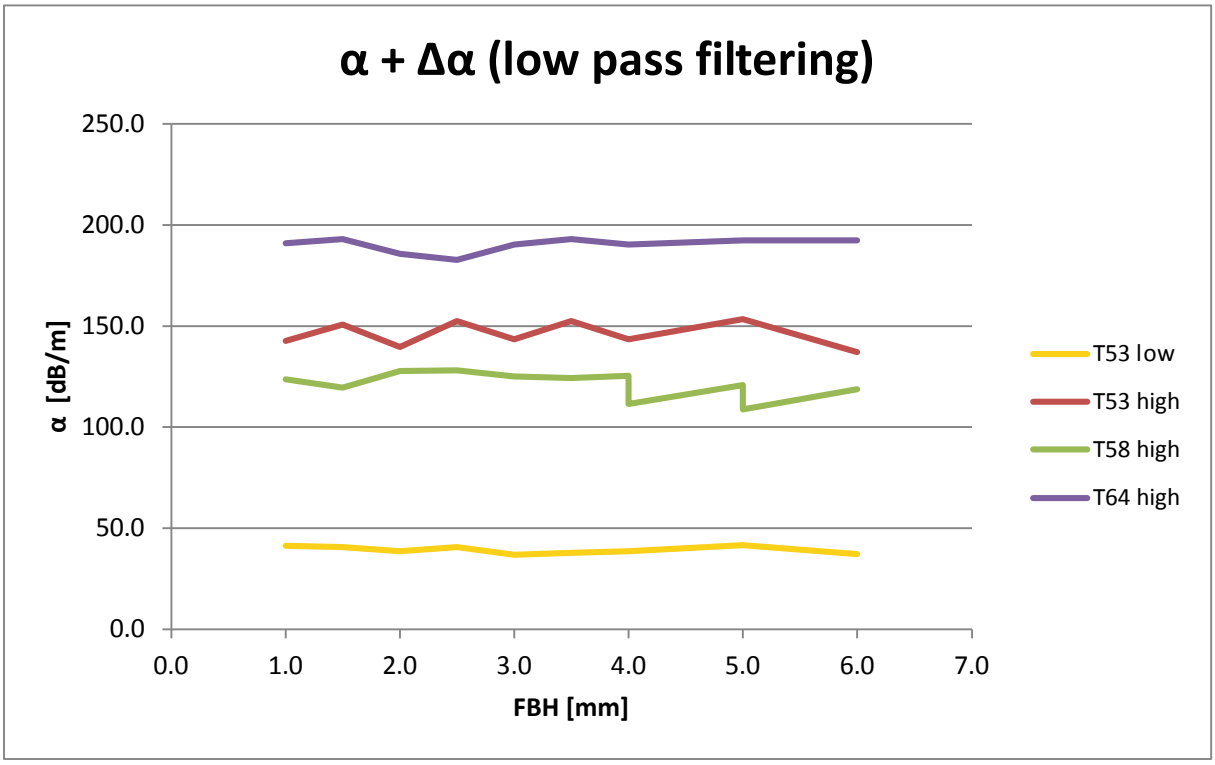

Figure 6-8. *Final local α from BWE difference including corrections by beam spreading, transmission loss and low pass filtering.*

6.2 Investigation of frequency dependence

The measurements by SKB, as shown in table 5-8 and 5-9, yield the frequency shifts of 12% to 34%., as listed in Table 6-1. The consequences are discussed here in more detail.

6.2.1 Change of the echo-amplitude

The modelling calculations were done for the nominal centre frequency of 3.5 MHz. If the frequency would be the same for the measured values then – beside the attenuation influence by $e^{-\alpha \cdot s}$ – the amplitudes for larger FBH diameters would have grown in a similar way for the modelled as for the measured values. One consequence of the lowered frequency of the sound waves reflected by the FBHs is that the measured echo amplitudes of this lowered frequency grow faster with FBH size than the modelled, where the frequency is higher, as it was observed in Figures 6-3 to 6-5. In case of zero attenuation the differences of the modelled amplitudes at the same depth are only caused by the different FBH diameters. The following diagrams were created in order to understand this deviation from the expected behaviour, as mentioned in the context of Figure 6-4.

In Figure 6-9 the modelled curve (for 3.5 MHz centre frequency) shows a type of saturation – which means that the slope becomes smaller and smaller for larger diameters while the measured amplitudes still grow proportional to the square of the diameter. One explanation could be that the measured values already follow far field behaviour due to the shift of the focus closer to the surface for lower frequencies.

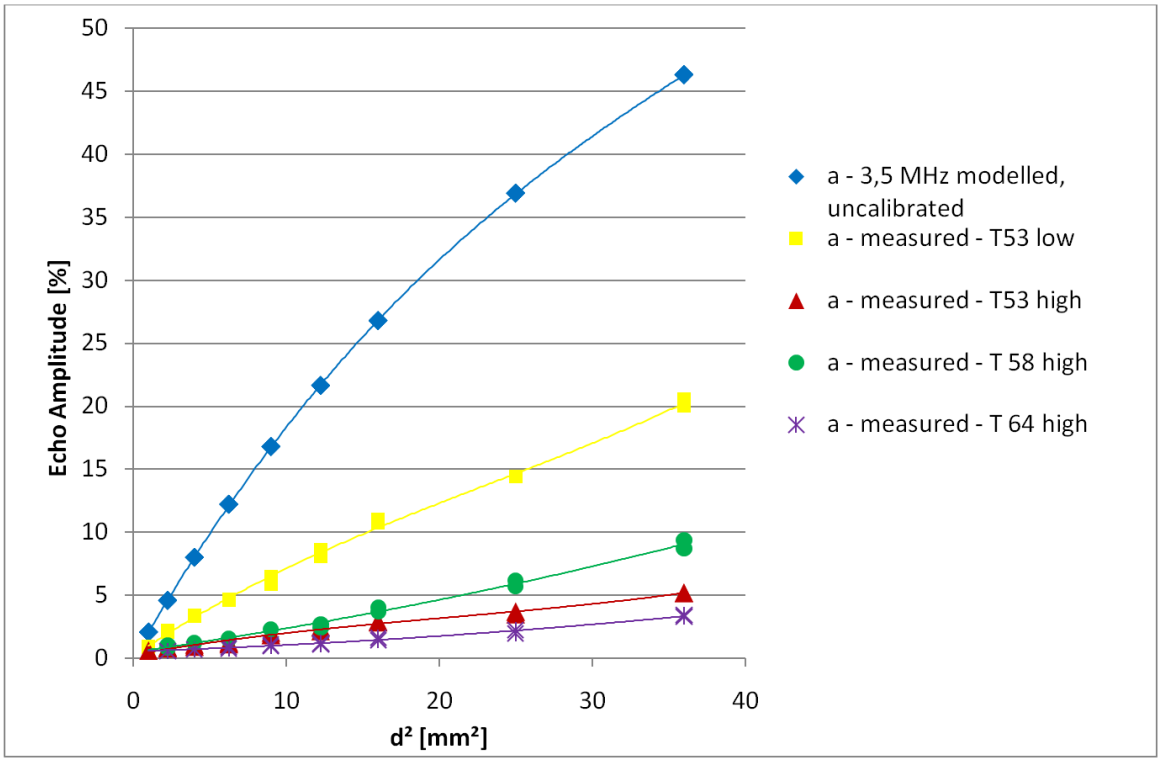

Figure 6-9. *Amplitude as function of FBH diameter squared. The model is not yet calibrated to the experiment. But it is seen that the modelled values for 3.5 MHz show saturation in the sense that the slope becomes lower and lower and the measured values still grow proportionally to the square of the diameter.*

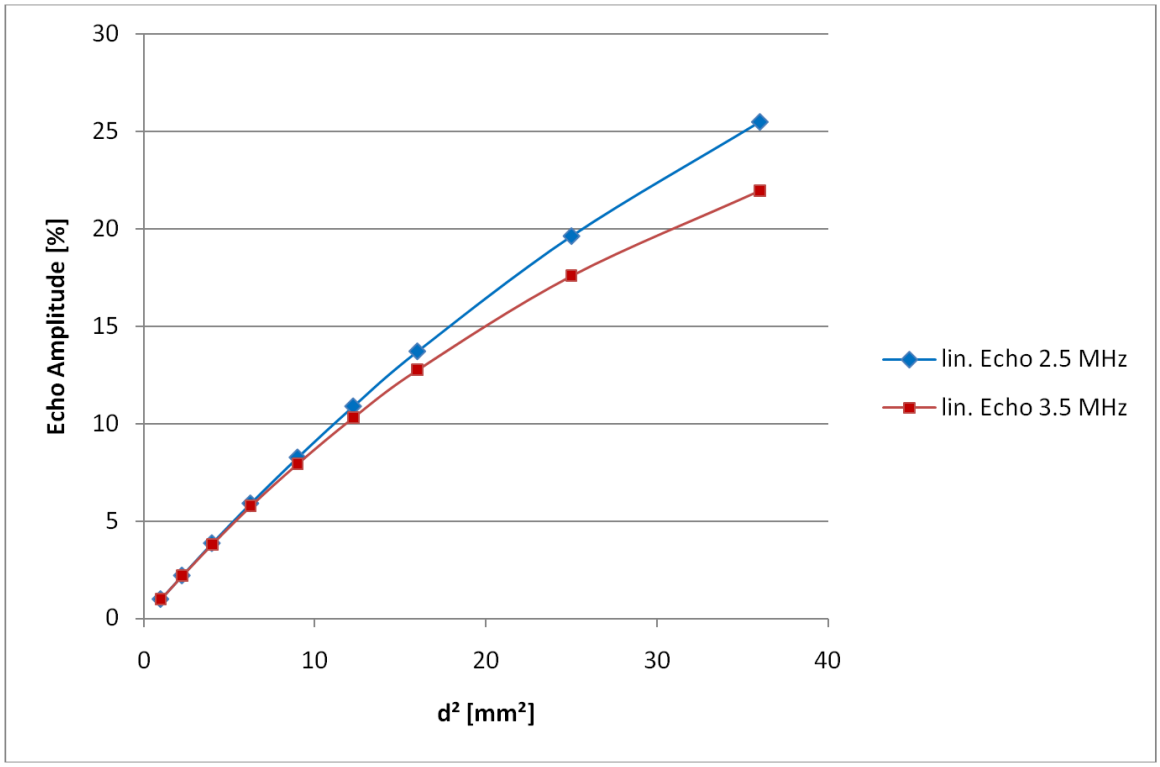

Figure 6-10. *Modelled amplitudes for 3.5 and 2.5 MHz frequency as a function of the FBH diameter squared. The 3.5 curve shows saturation (lowered slope from diameter to diameter) and the 2.5 curve is still growing proportionally to the square of the diameter, as in the far field behaviour.*

The modelled results depicted in Figure 6-10 confirm the explanation of the deviation in Figure 6-8. In the Figure 6-10 we see the modelled sound pressure as a function of depth in mm. The green curve represents the 3.5 MHz probe with a focus depth of 40 mm, and the blue one the 2.5 MHz probe with a focus depth of 30 mm.

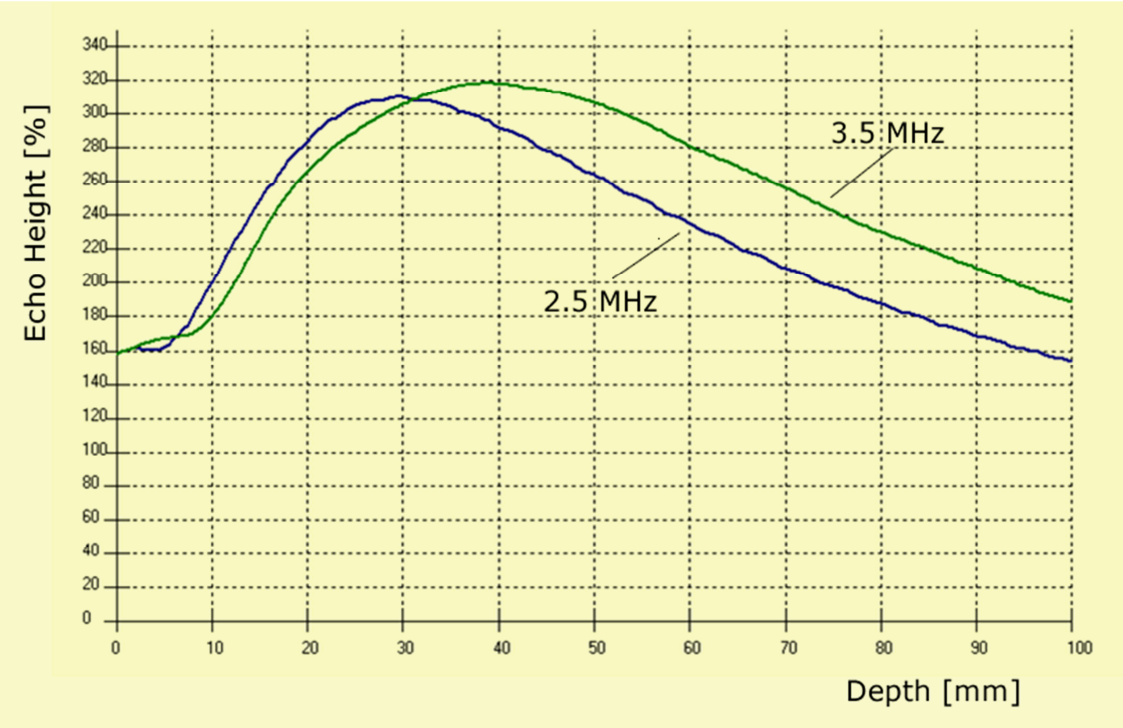

Figure 6-11. *Sound pressure along the symmetry axis of the probe (depth) for 3.5 MHz (green) and 2.5 MHz (blue). For 2.5 MHz the maximum is shifted to a lower distance and shows far field behaviour in 49 mm distance, i.e. with respect to the distance the amplitude falls proportional to the inverse of the distance.*

6.2.2 Consequence of the low pass filtering effect on the BWE

In this sub-chapter the effect of frequency filtering by the grain size distribution on the attenuation and the first and the second back wall echo is considered.

In order to investigate the attenuation and the frequency shift of the ultrasonic waves as a function of depth for different grain size distributions, a set of test specimens from the T53 tube were manufactured, as seen in Figure 4-4. On these step wedges specimen BWE and FFT measurements were carried out, as described in chapter 5.1.3. The measurement results are summarized in Table 5-11 whereas the calculated attenuation coefficients are shown in Figure 6-12 and summarized in Table 6-6. The calculation was carried out using the correction for beam spreading according to Table 5-14 and the transition loss, by the use of the theoretical value based on the difference of acoustical impedances, the between copper and water of -0.63 dB (0.93 lin.). This value has been applied once for the first BWE, three times for the second BWE and five times for the third BWE. *Remark: for the current evaluations the value measured by BAM for the losses of 1.5 dB was used (equals two times 0.75) in the difference between second and first BWE and so on.*

From these tables and figures above it can be seen that there is a moderate frequency shift and change of α in the specimen for T53low outer and inner and also T53high outer part with the tendency expected from Figure 6-2. For T53high inner part this behaviour is overwritten by additional inhomogeneity in the depth direction of the tube, which indicates on a concentration of high grain sizes near the inner surface of the T53high sample.

In addition the specific values for α could still change when the beam spreading corrections for the actual frequency according to the last column in Table 5-11 will be considered. The beam spreading correction is especially sensitive around the focus area and the focus is shifted considerably for the lowered frequency, as indicated in Figure 6-11

Table 6-6. α values determined from BWE1 and BWE2 (α1) and BWE2 and BWE3 (α2) for the above measurements.

Sample	Depth (mm)	α1 [dB/m]	α2 [dB/m]
T53-960-125 Step 17	17	55	0
T53-960-125 Step 34	34	96	
T53-960-125 Step 49	49		
T53-1030-125 Step 17	17	216	96
T53-1030-125 Step 34	34	105	
T53-1030-125 Step 49	49	59	
T53-960-220 Step 17	17	36	0
T53-960-220 Step 34	34	28	
T53-960-220 Step 49	49	71	
T53-1030-220 Step 17	17	49	19
T53-1030-220 Step 34	34	26	
T53-1030-220 Step 49	49	61	

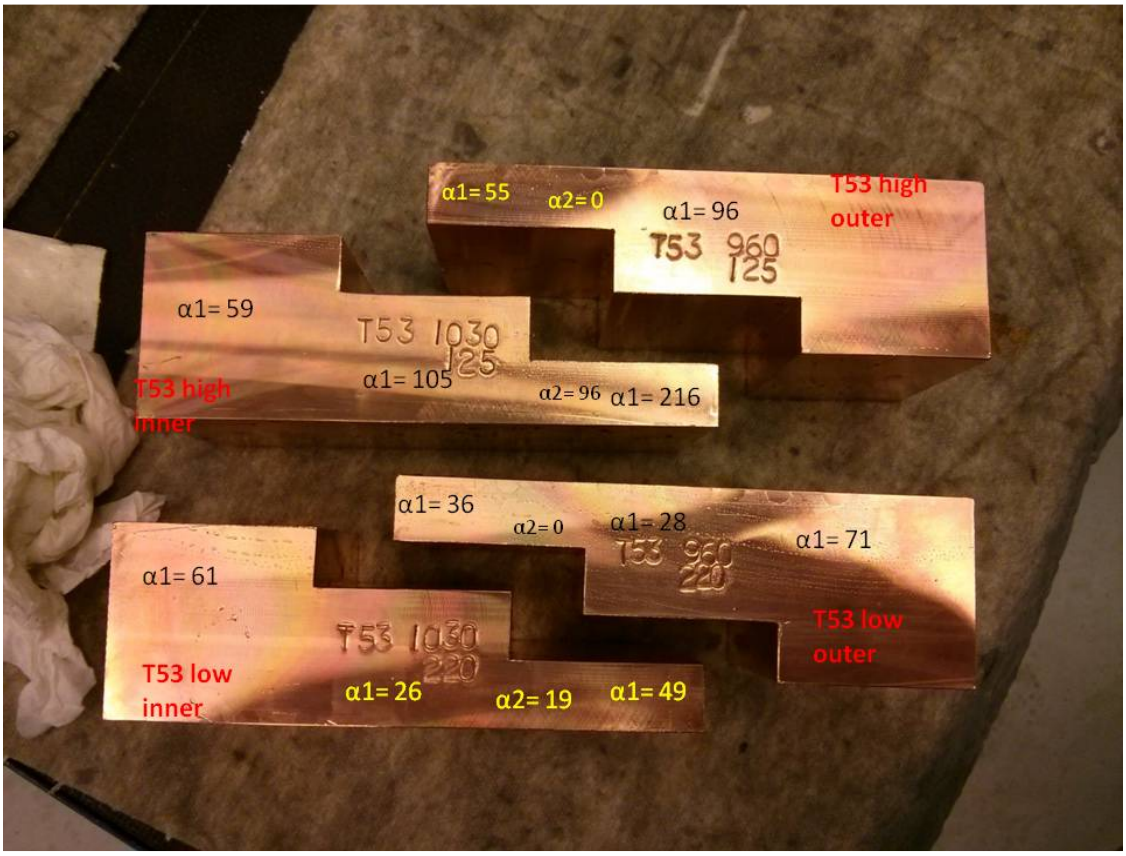

Figure 6-12. *Step wedge test specimen from low and high attenuation regions in T53.*

6.3 Multi-parameter POD calculations

The basic data set is used as an input for the POD evaluation according to Berens (1989), using a MatLab computer code. Since the values for the 6 mm FBH (the last one in the upper right corner in Figure 6-13) do not fulfil the pre-condition of homogeneous scatter, it was excluded from the further calculations. This can be further elaborated through the observation that the amplitude from the 6 mm FBH is already far in the saturation of the POD curve. This means that this action shall not influence the detectability in the sensitive region where the POD is growing. This problem might not occur when the modelling calculation would be repeated for lower frequencies.

Figure 6-13 shows the *α cleaned* basic data set in $\hat{a}$ versus a-format with, and the Figure 6-14 without the 6mm FBH. In the Figure 6-15 (Minimum), Figure 6-18 (Medium) and Figure 6-21 (Maximum) the $\hat{a}$ versus a diagrams for the attenuation scaled ($\cdot\, e^{-\alpha \cdot s}$) measured and modelled amplitudes are shown. The Figures 6-16, 6-19 and 6-22 show the corresponding POD curves as a function of the modelled amplitude, where the decision threshold of 3 times the noise level was applied (~1.2 in linear scale). In the Figures 6-17, 6-20 and 6-23 the PODs are plotted against the FBH diameter. The corresponding FBH diameters are determined from the reversal of the modelled sound field values. (Practically this means in the Tables 6-2 to Table 6-5, after rescaling the attenuation the modelled amplitude can be found in column 10 and the corresponding diameter in column 3). The corresponding d90/95, in terms of the detectable FBH diameter, is indicated in the captions of the figures and summarized in Table 6-7.

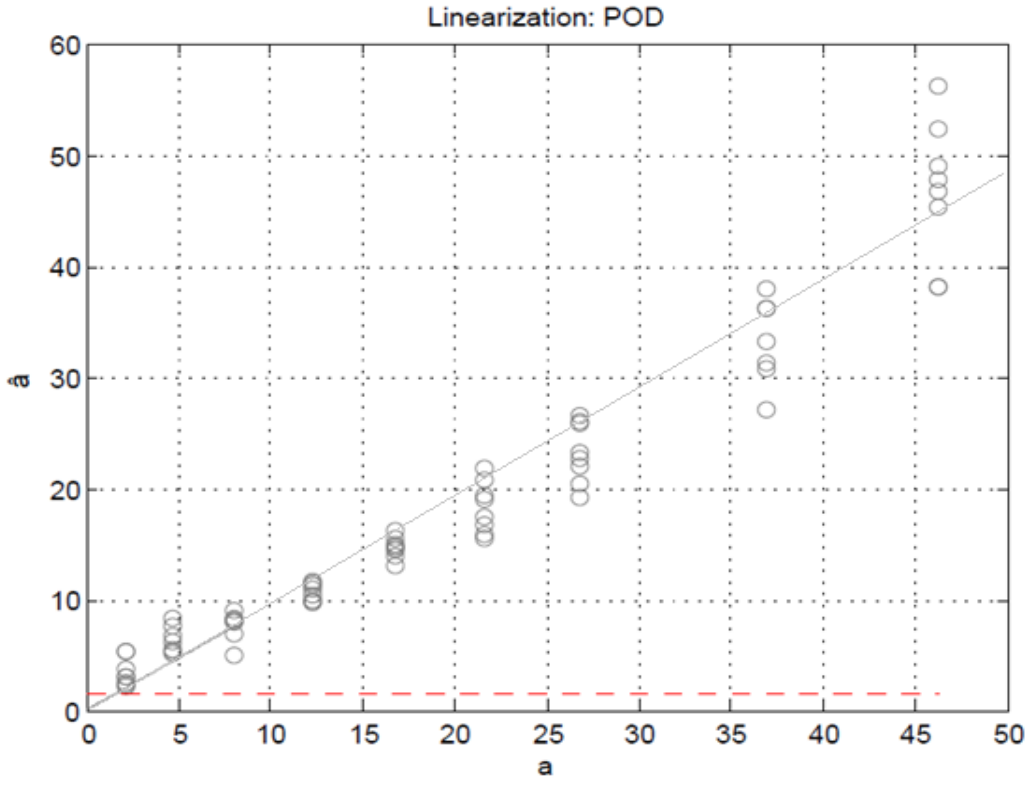

Figure 6-13. *â over a (without α) decision threshold 3X noise level, all values shown in percent.*

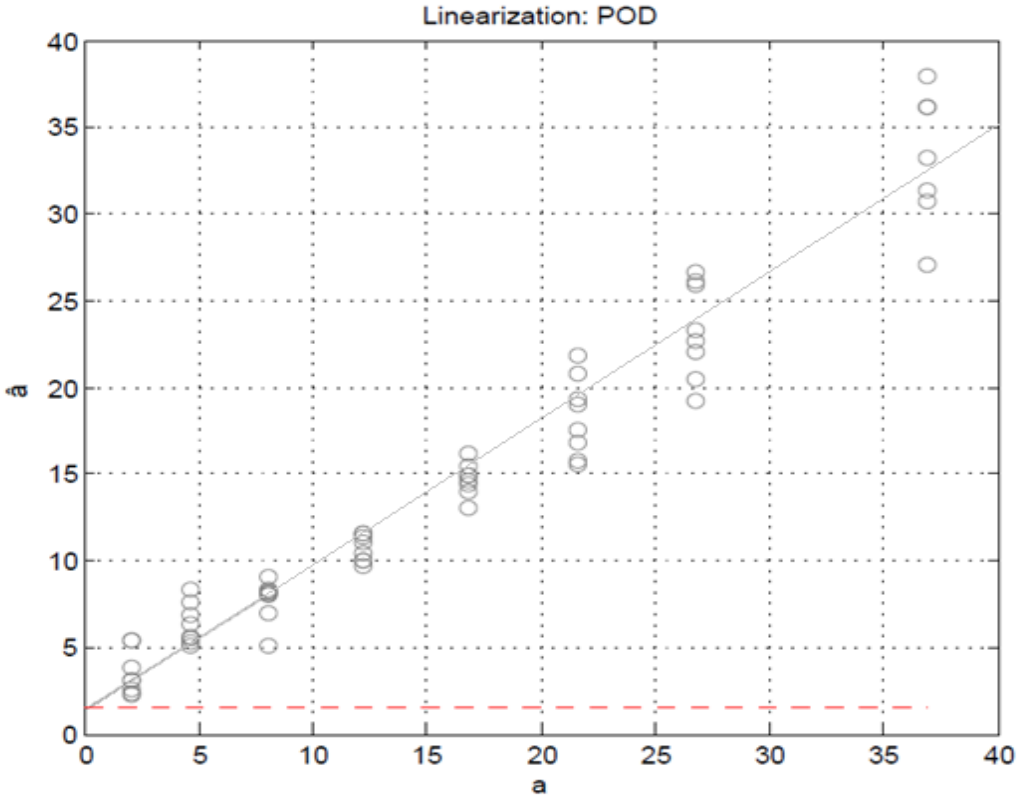

Figure 6-14. *â versus a (α cleaned and 6 mm FBH excluded), all values shown in percent.*

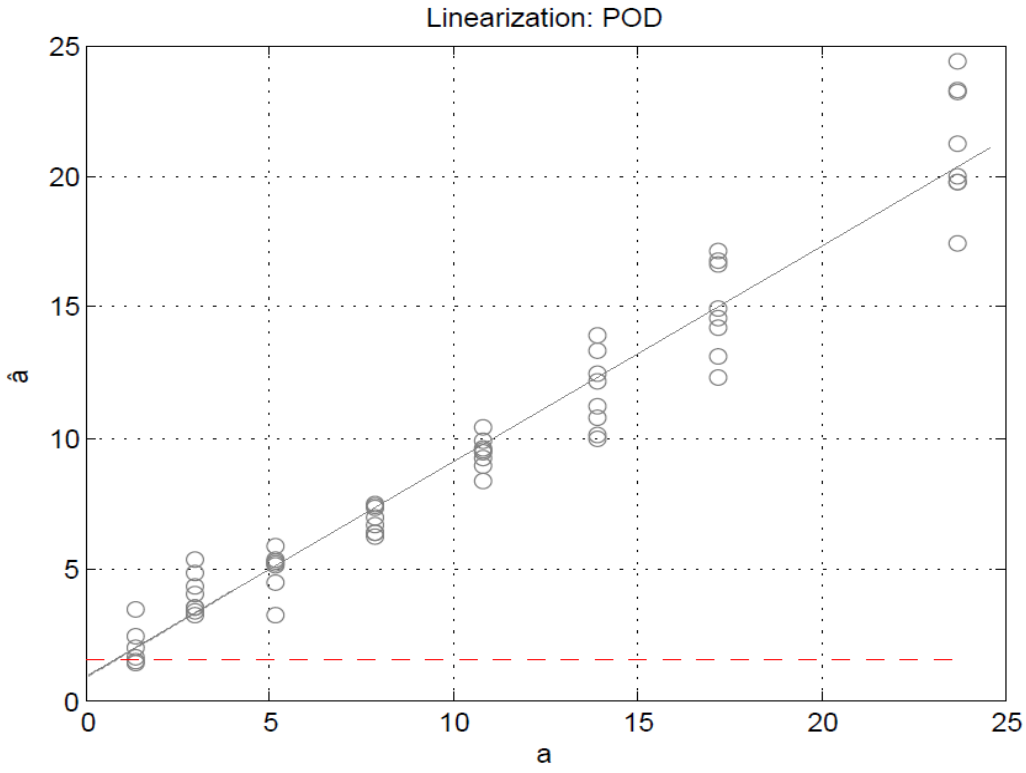

Figure 6-15. *â over a Minimum α (39.2 dB/m), 6 mm FBH excluded, all values shown in percent. Decision threshold 1.73%.*

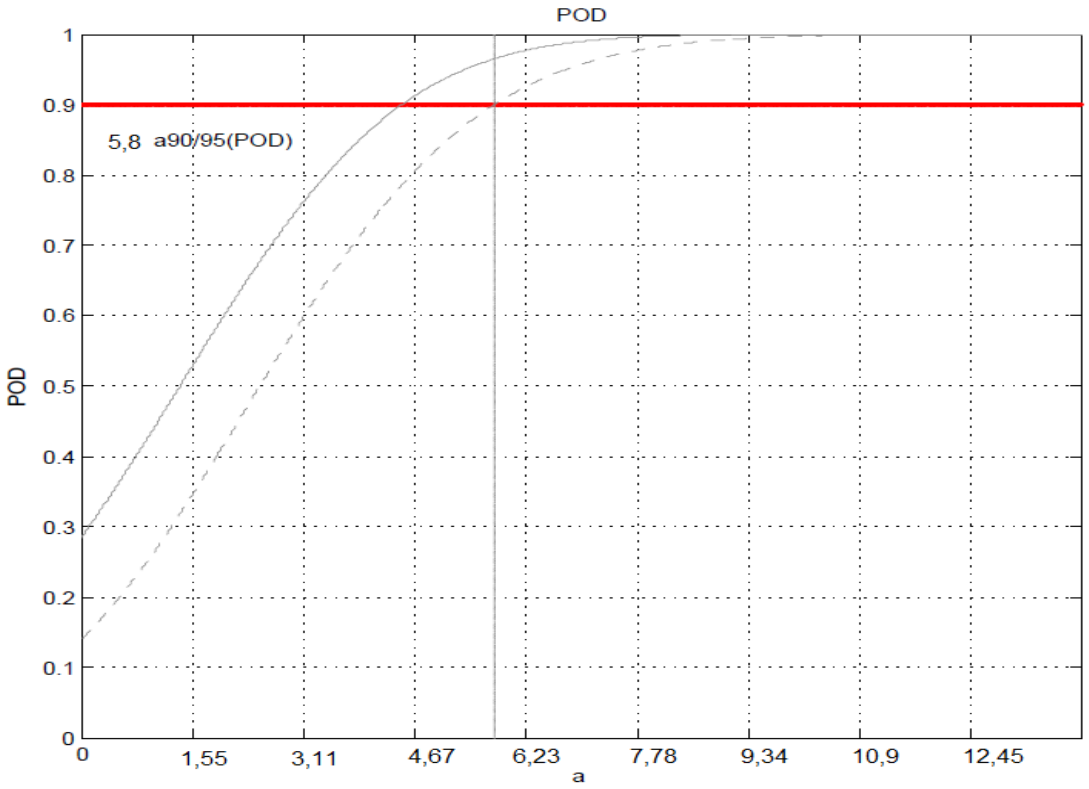

Figure 6-16. *POD Minimum α, a [mm^2].*

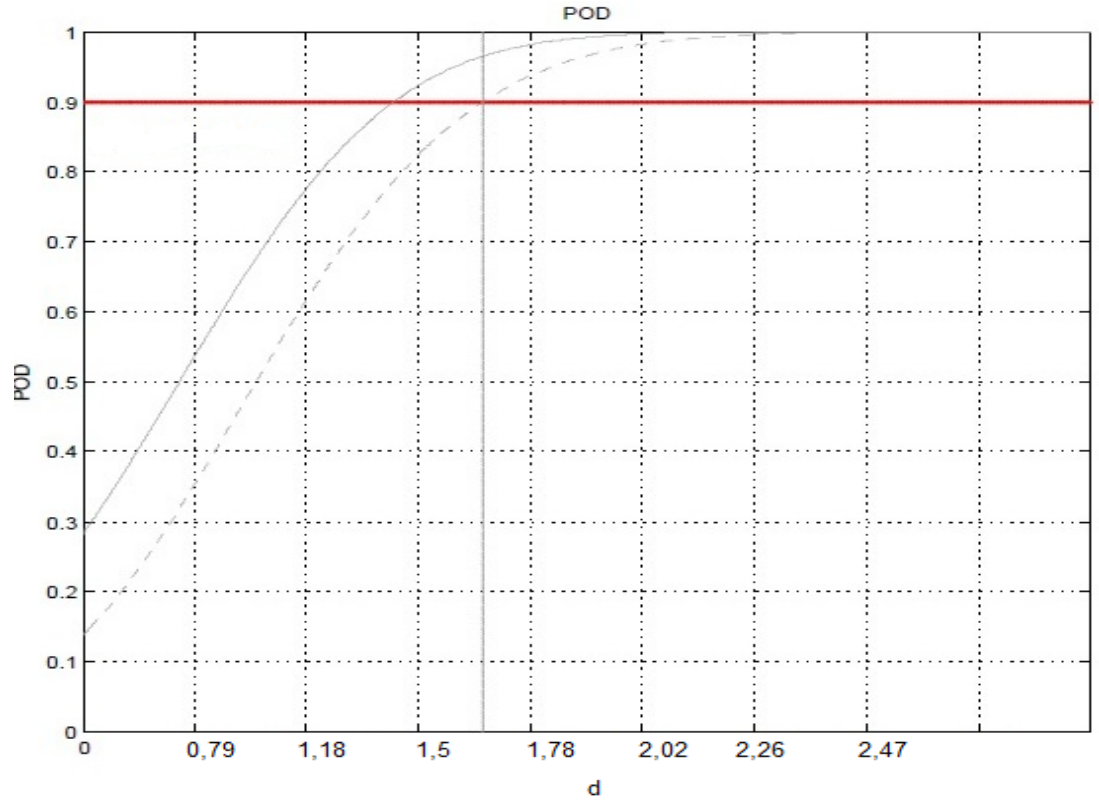

Figure 6-17. *POD Minimum α (39.2 dB/m) in dependence on the diameter d (flat bottom hole diameter), d90/95 ~1.66 mm.*

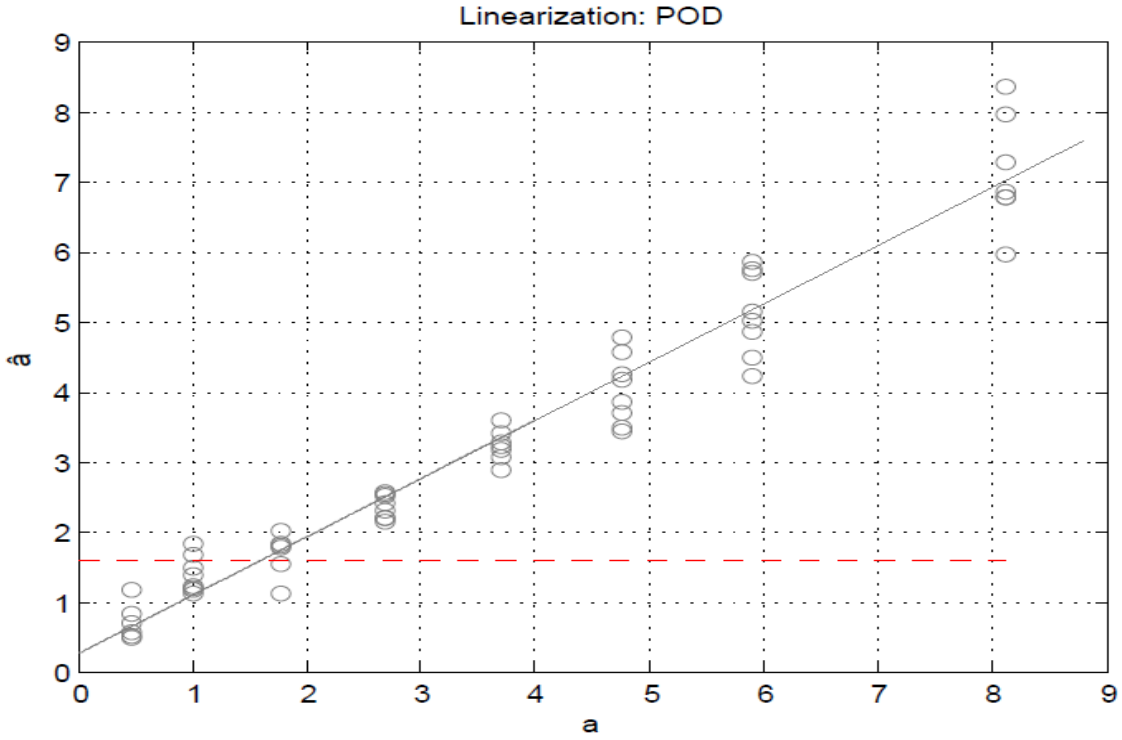

Figure 6-18. *â versus a Medium α (134.2 dB/m) 6 mm excluded, all values shown in percent.*

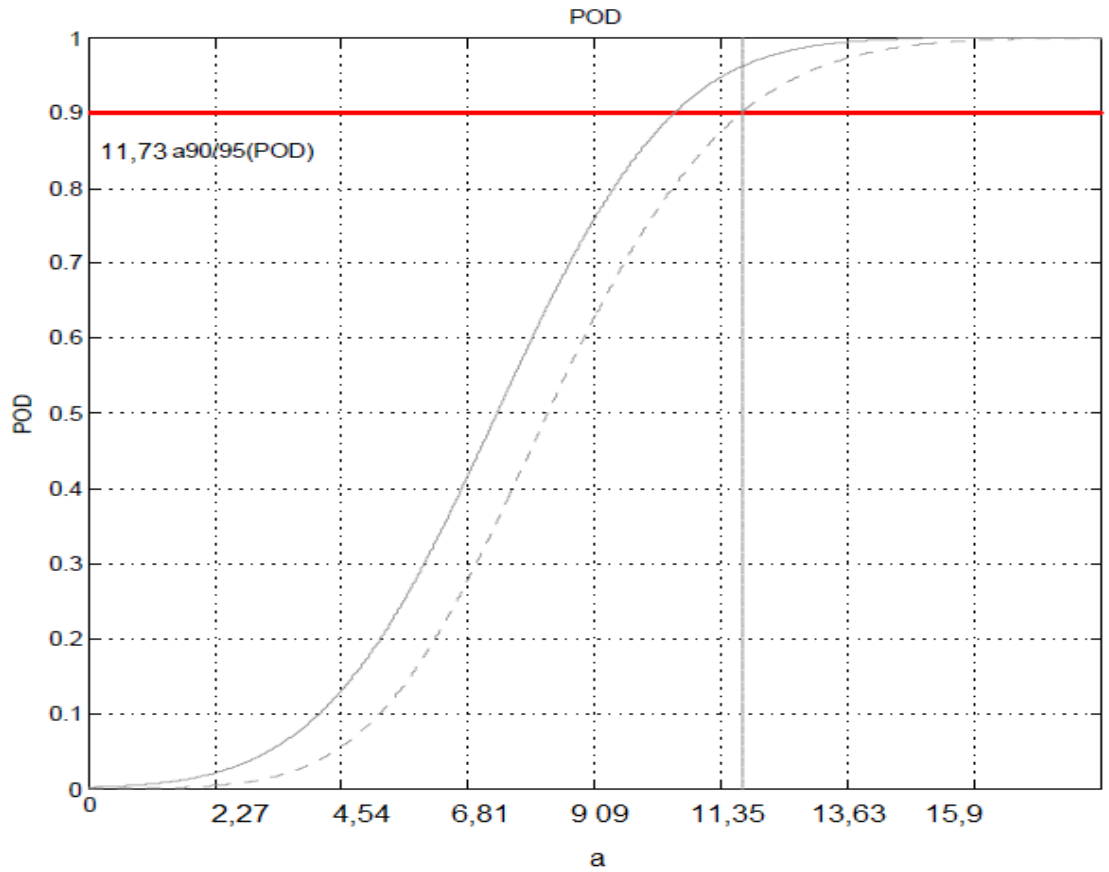

Figure 6-19. *POD Medium α, a [mm^2].*

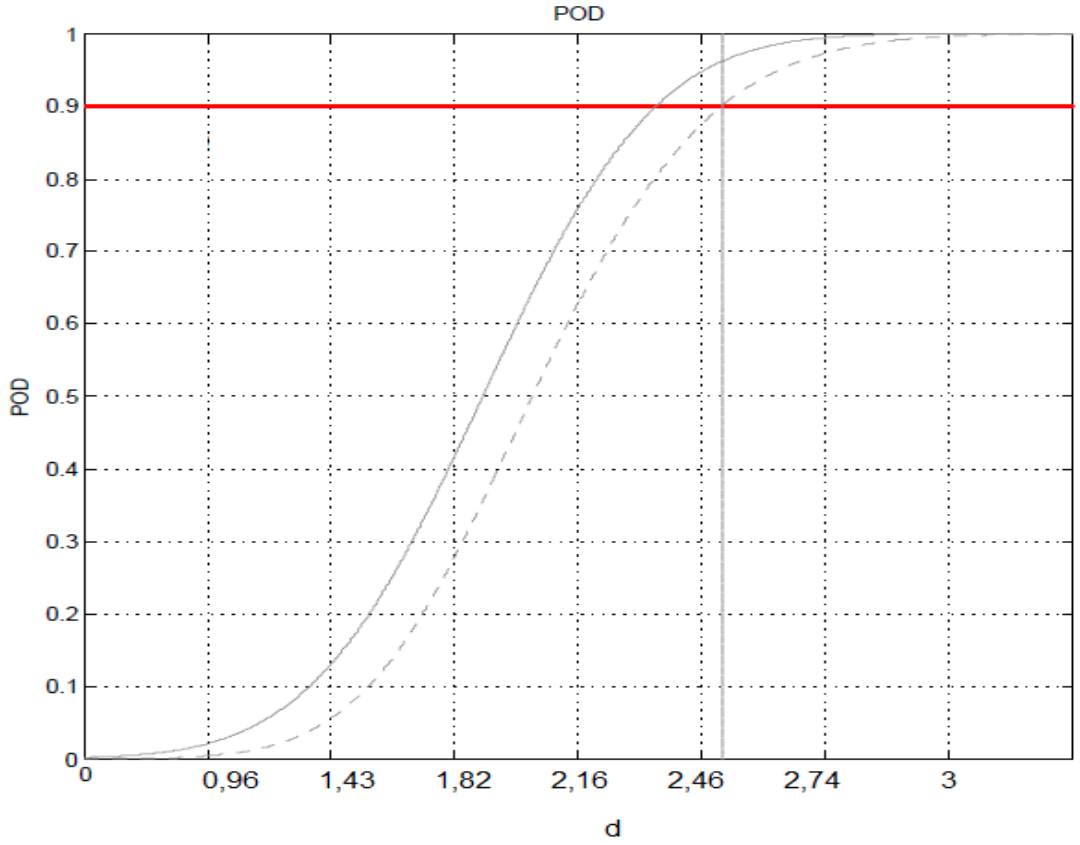

Figure 6-20. *POD Medium α (134.2 dB/m) as a function of FBH diameter d, d90/95 ~ 2.51 mm.*

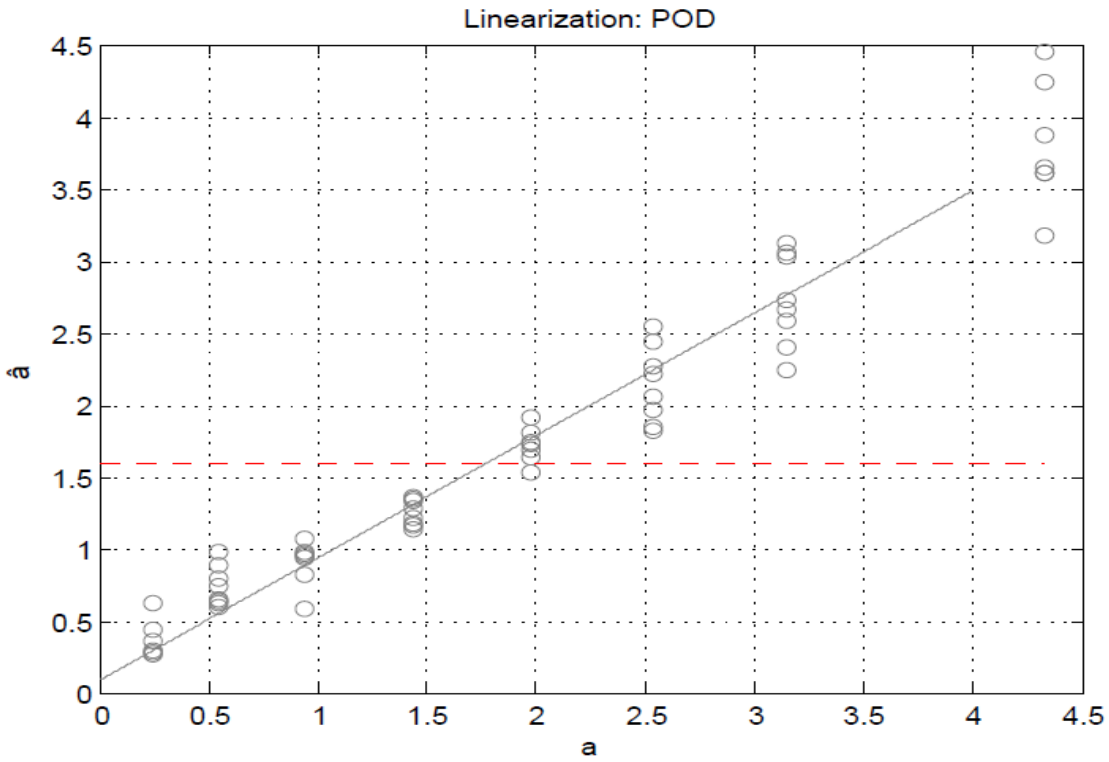

Figure 6-21. *â versus a Maximum α (189.9 dB/m), all values shown in percent.*

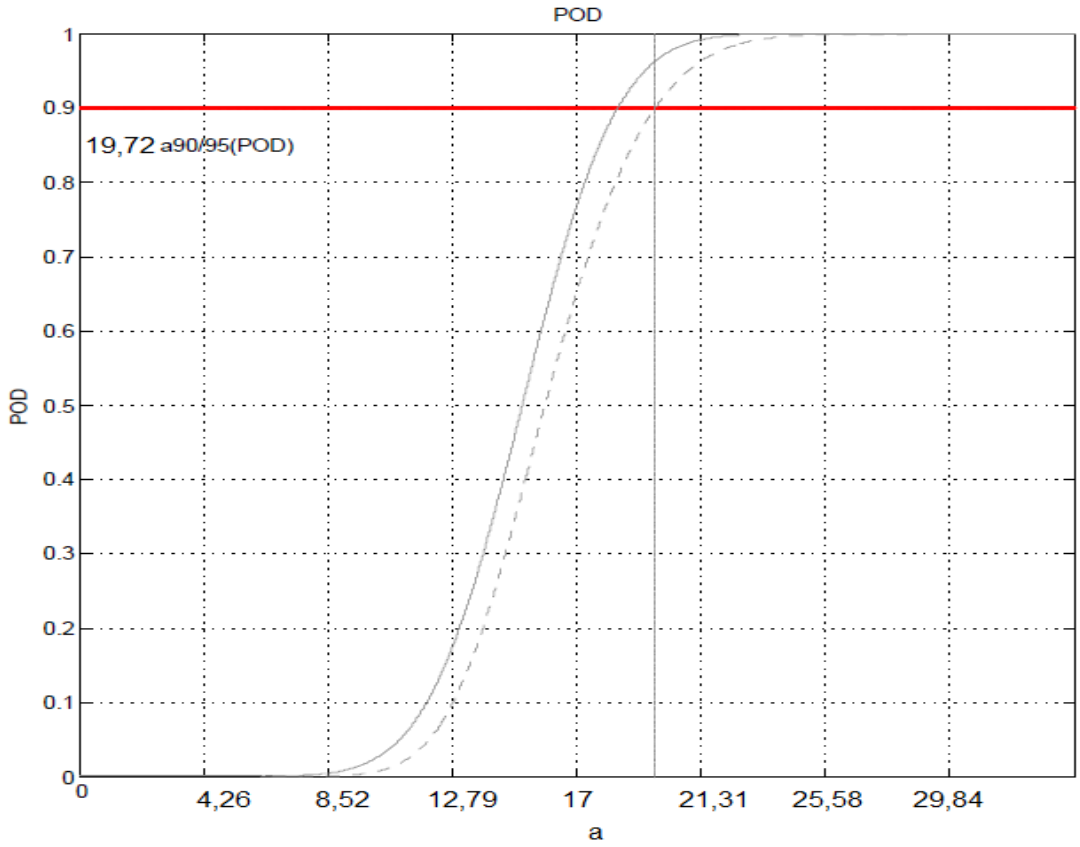

Figure 6-22. *POD Maximum α, a [mm²].*

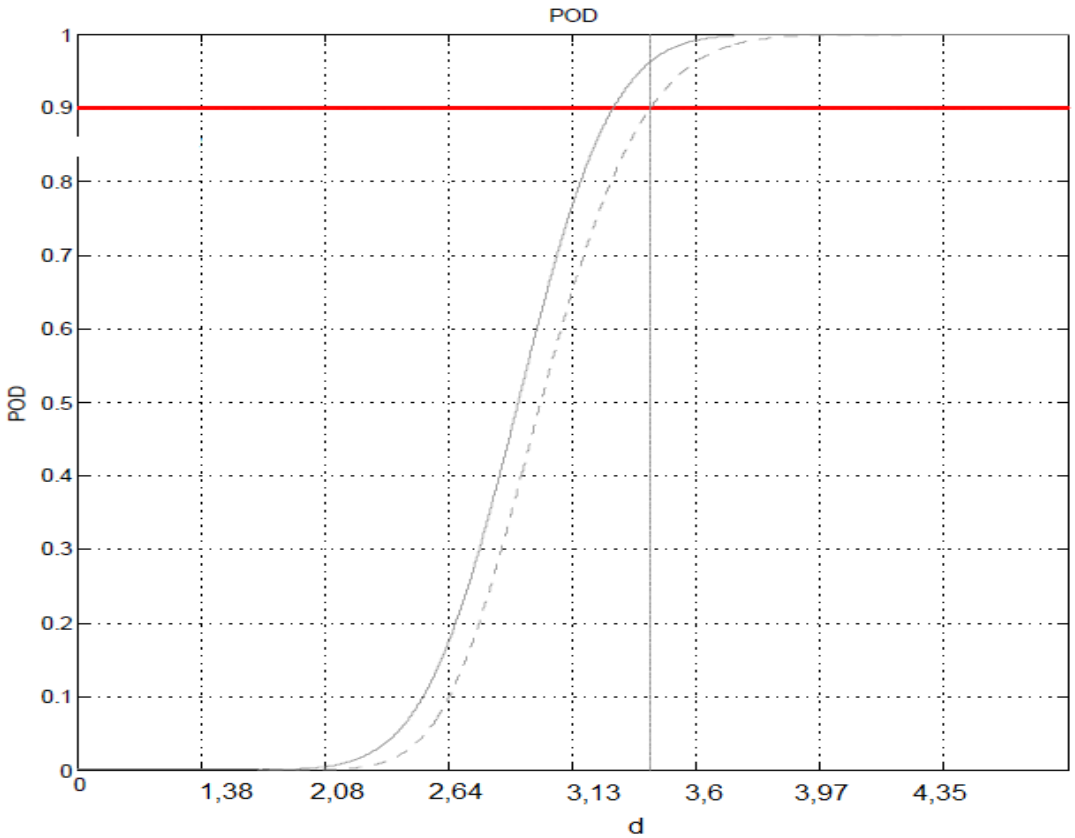

Figure 6-23. *POD Maximum α (189.93 dB/M) as a function of FBH diameter d, d90/95 ~ 3.41 mm.*

6.4 Multi-parameter POD results

The final results for the multi-parameter POD, as presented in the Figures 6-13 – 6-23, are summarized in Table 6-7 and in Figure 6-24.

Table 6-7. Minimum, medium and maximum attenuation values and corresponding detectable (d90/95) diameters. The last column shows the corresponding mean BWE from the measurements. The Super Maximum* in the last row is a fictive highest attenuation value.

	α [dB/m]	d90/95 [mm]	Mean BWE [%]
Minimum	38.2	1.66	43.43
Medium	134.2	2.51	12.17
Maximum	189.9	3.41	6.33
Super Maximum*	275	5.5	

It can be observed that the growing attenuation from about 50 dB/m up to about 200 dB/m is reflected in a highly diminished BWE-height, as well as in the growth of the detectable defect from less than 2 mm to more than 3 mm. This is still sufficient and the integrity of the tube is not affected. Utilizing the opportunity for scaling measured values and modelled amplitudes with arbitrary attenuation, a very high α of 275 dB/m was postulated and with this theoretical α a POD as a function of FBH diameter (d90/95) of 5 mm was calculated, The actual α variations are in the same order of magnitude, as mentioned by Stepinski et al. (2009), where the attenuation in the extruded copper parts varies from ~70 dB/m to ~200 dB/m at 3.5 MHz. This shows that our mathematical-physical concept of $\alpha = \alpha 0 + \Delta\alpha$ is applicable for the current copper materials and the broad band phased array ultrasonic technique. Still, further confirmation by ultrasonic experiments and grain size measurements are desirable.

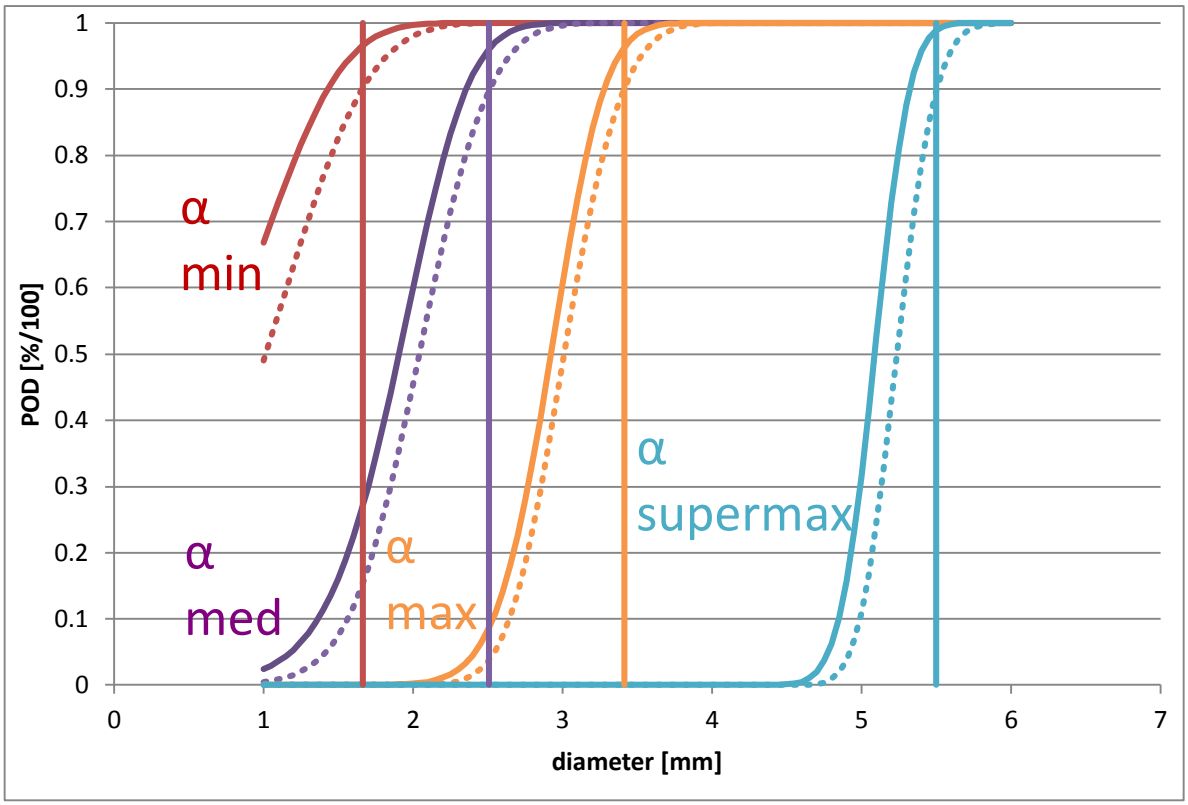

Figure 6-24. *Summary of the calculated POD for α min, α med, α max and the postulated α supermax as a function of FBH diameter with indicated d90/95 values.*

7 POD0 (one-parameter POD) Analysis and Results

In chapter 6 the α values for the region between the surface and the defect were determined using the modelling-based adaption that the measured echo amplitude $\hat{a}$ should form over the model an ideal line in case they are calibrated according to the correct attenuation. Because this is not yet verified by experimental results for the correct value of attenuation between the surface and the defect, we aim to compare our results for the POD and d90/95 values for the different α with the empirical one-parameter POD results. The application of the one-parameter POD is possible, when the POD is considered as a function of the square of the diameter (far field behind a FBH) for each tube segment separately. The $\hat{a}$'s are the censored measured amplitudes and the a's are the d^2 (square of FBH diameter) values as listed in column 8 and 3 of Table 6-2 to Table 6-5. These data are again used as input data for the POD –program, mentioned earlier, together with the decision threshold of 3 times the mean noise level, as before.

Figure 7-1 to Figure 7-8 show the corresponding empirical $\hat{a}$ versus a and the POD0 results including the d90/95 value for the detectable diameter.

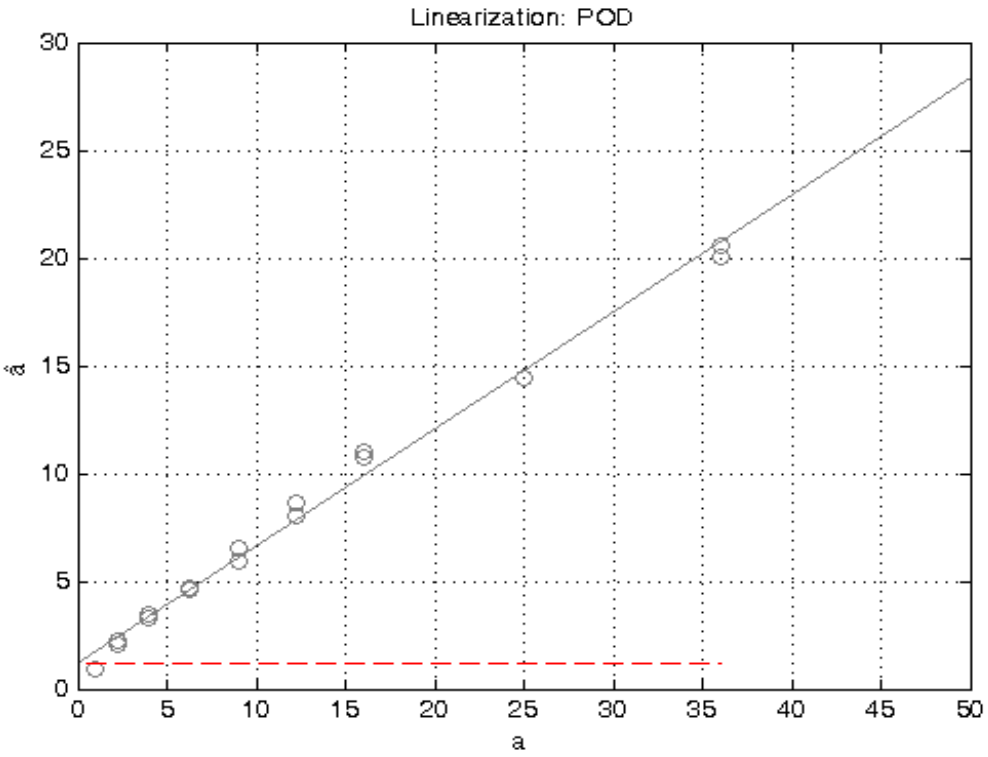

Figure 7-1. *â versus a diagram for T53low attenuation, â in percent screen height and $a=d^2[mm^2]$.*

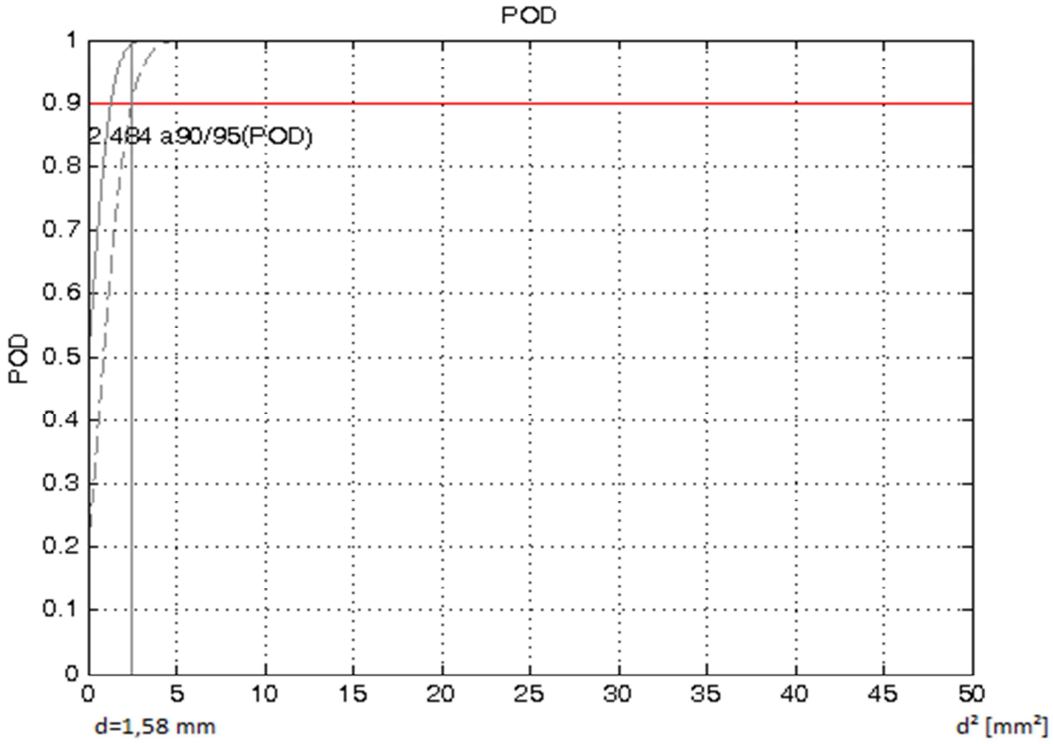

Figure 7-2. *POD (d^2) for T53 low attenuation.*

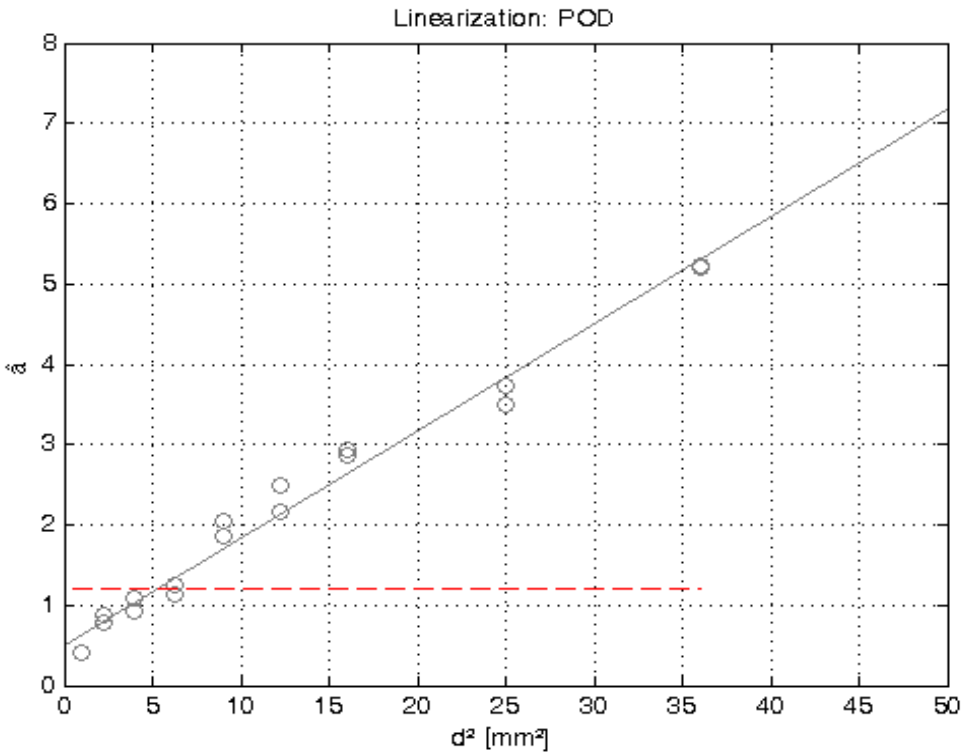

Figure.7-3. *â versus a diagram for T53high attenuation. â in percent screen height and $a=d^2$.*

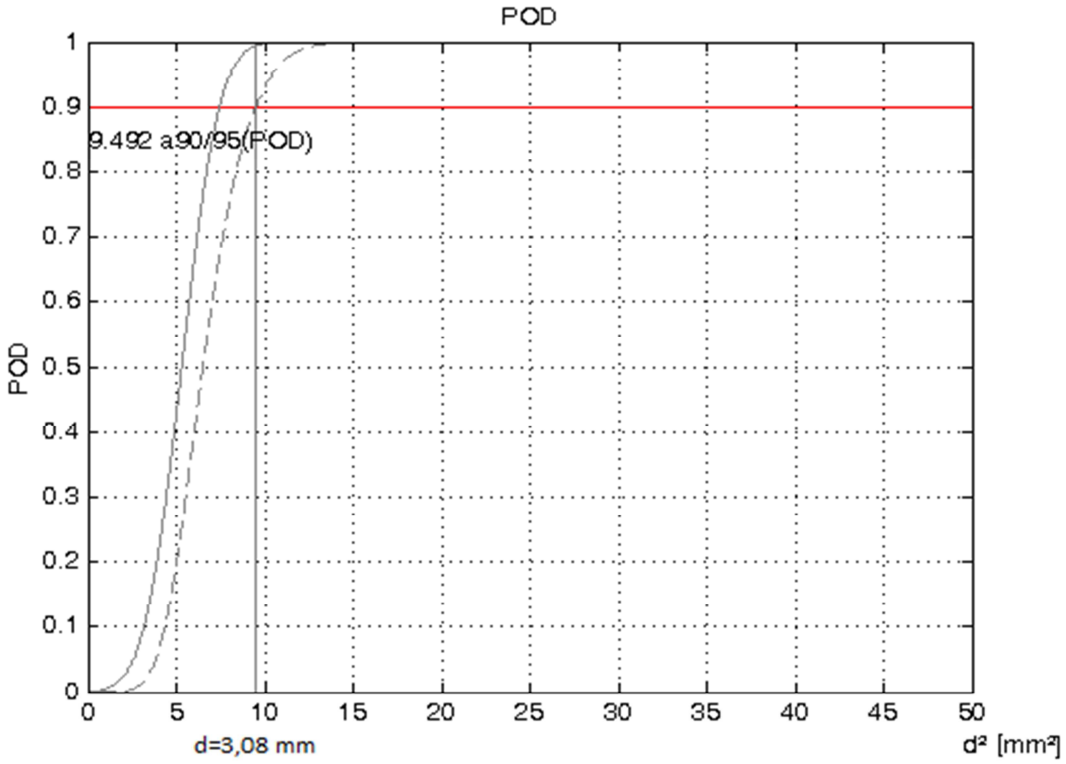

Figure 7-4. *POD(d^2) for T53 high attenuation.*

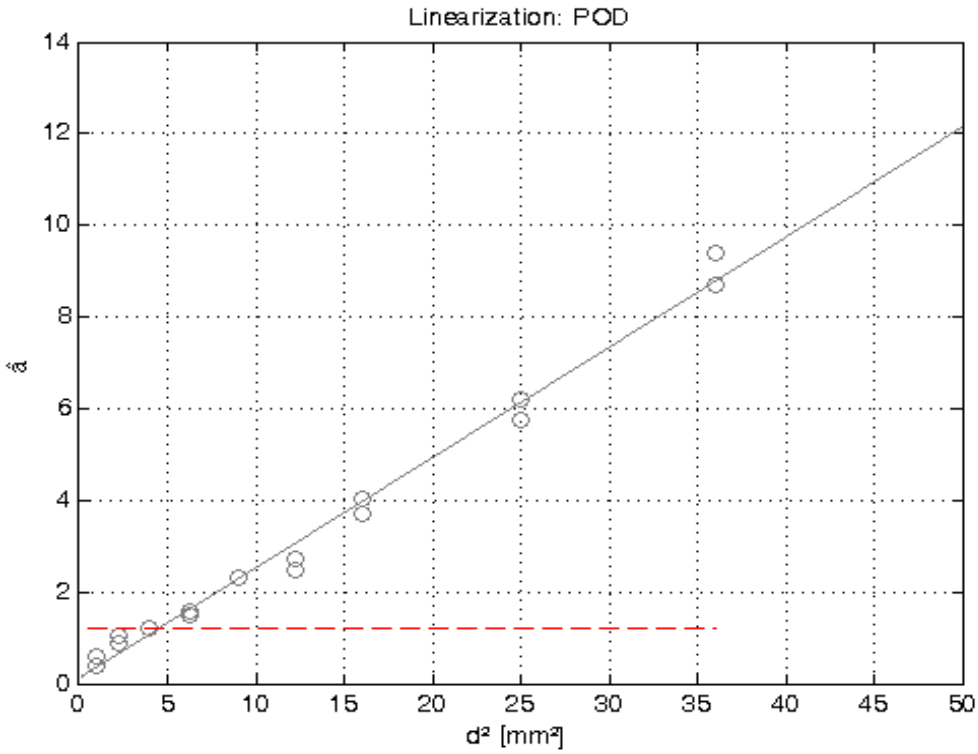

Figure 7-5. *â versus diagram for T58 high attenuation. â in percent screen height and a=d.*

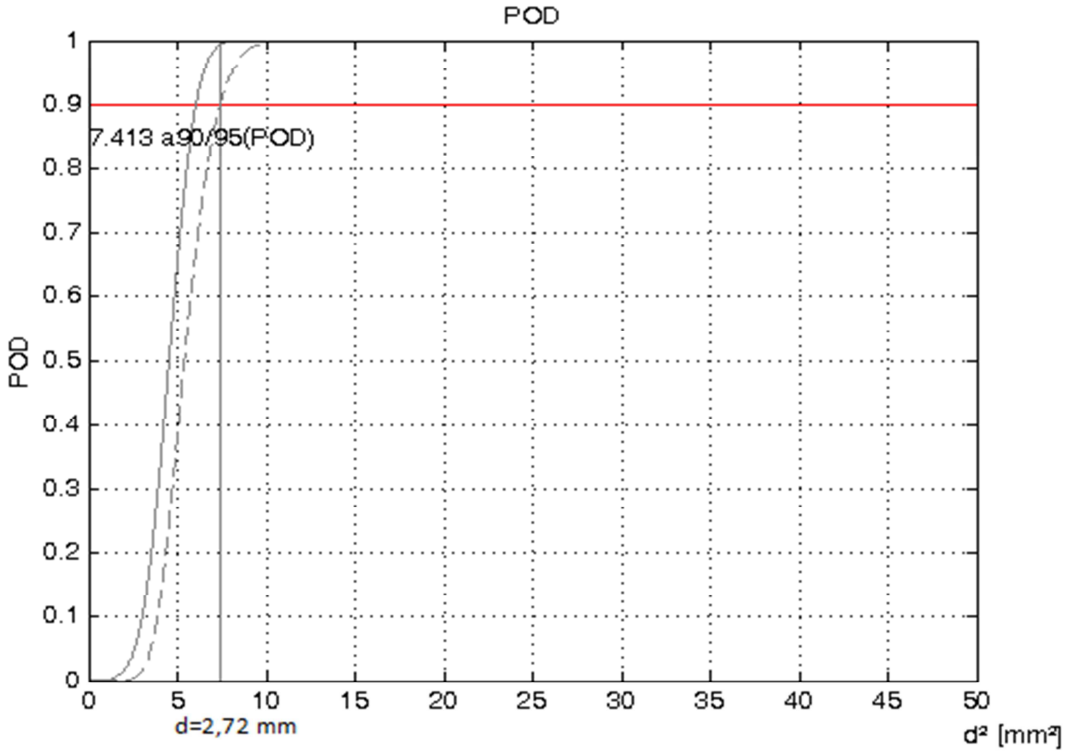

Figure 7-6. *POD (d^2) for T58 high attenuation.*

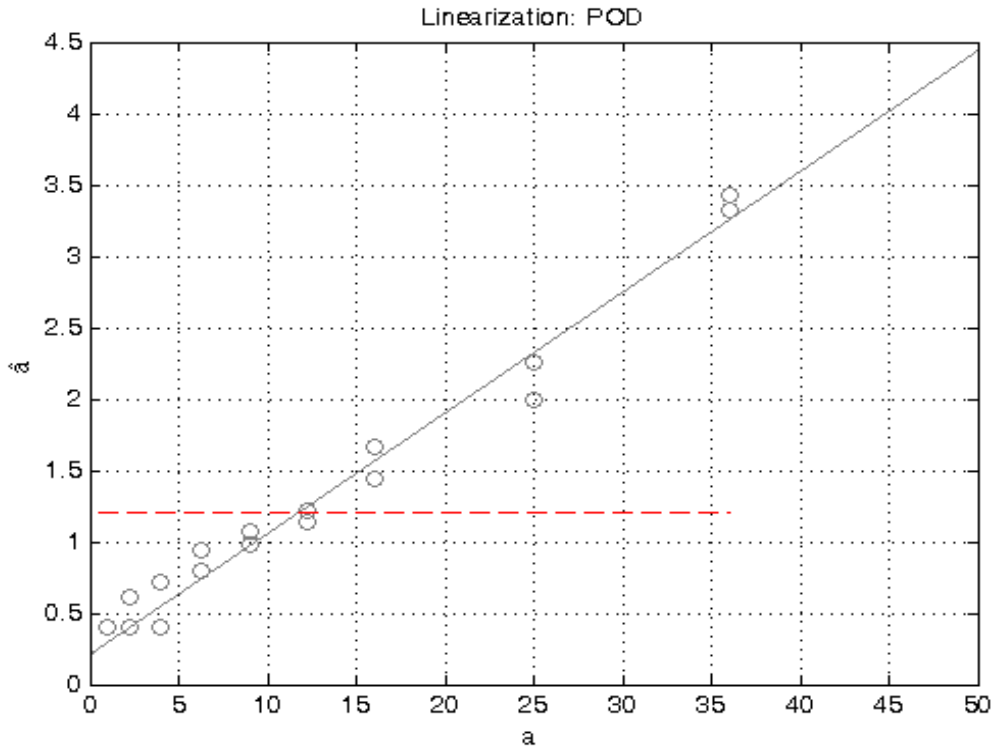

Figure 7-7. *â versus a diagram T64 high attenuation, â in percent screen height and $a=d^2$.*

.

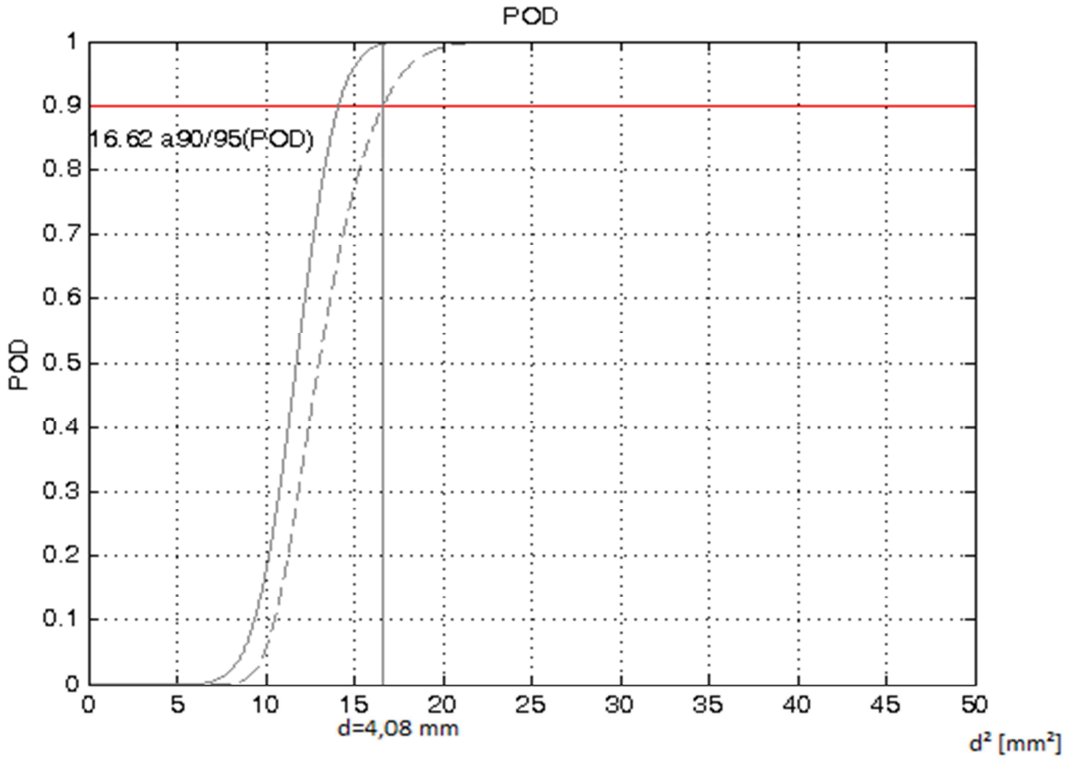

Figure 7-8. *POD (d^2) for T64 high attenuation.*

Table 7-1. Results for POD0: For the nine FBH's the censored amplitude against d^2 was fitted in an empirical signal response POD for each tube segment separately

Tube section	α (assessment from multi-parameter-approach) [dB/m]	Detectable diameter d90/95 [mm] with the multi-parameter result in parentheses	Mean BWE
T53 low	39.2	1.58 (1.66)	43.40%
T58 high	122.2	2.72 (2.51)	10.82%
T53 high	146.1	3.08 (51)	13.52%
T64 high	189.9	4.08 (3.41)	6.33%

The d90/95 for T53low is comparable with the results from the multi-parameter POD, but for higher attenuated material the values are higher, even though they are in the same order of magnitude. The higher d90/95 values might be due to the broader confidence bounds due to the lower amount of available data in comparison to the multi parameter results. The fact that the sound field with its focal law is taken into account only in the multi-parameter approach, explains why the calculation yields better results for it. This advantage will be of special interest when the defect depth is varied.

In principle, this POD0-calculation supports the multi-parameter approach because the relation between the signals and the thresholds is repeated here with the original values for T53low, T58high and T53high and T64high as for the scaled values for low, medium and high attenuation. Furthermore, the advantage is seen in the higher statistical basis in case of the multi-parameter data set.

8 Discussion

During the data analysis it turned out that the attenuation is not only dependent on the surface position of the copper tubes, but also on the depth position as the actual grain size distribution cause a low pass filtering of the ultrasonic signal. The frequency shift between the surface echo and the first BWE varied from 12% for the lowest attenuating material up to 34% for the highest attenuating material. As a consequence, the differences between the second and the first BWE were not sufficient to determine the local attenuation, which affects the UT-wave responsible for defect detection. The remaining difference in attenuating coefficient (α) was determined by a model assisted iteration assuming that the modelled amplitude and the measured amplitude should form a 45° line, when both contain the correct α, or vice versa - when both are renormalized by the correct α. Additional experiments are necessary for the final verification of the approach. For example, the difference in attenuation coefficient between the measured and the modelled data for the low attenuated material was set to 0 dB/m. But if the frequency shift of 12% from surface echo to the first BWE had been considered, it would be more realistic to set the $\Delta\alpha$ to a value greater than zero.

In the literature (Stepinski et al. 2009) the relation $\alpha \sim D^3 \cdot f^4$ is given where D is the mean grain diameter and f the frequency, which shows that even a small frequency shift causes a remarkable change in α. From table 6-1 it can be seen that the frequency after the BWE was lowered by a factor of 0.88 for T53low, 0.81 for T58high, 0.72 for T53high and 0.64 for T64high (SF), i.e. the original frequency was higher by the reciprocal factor. This means that the α near the surface was higher by the factor $(1/SF)^4$ than after the first BWE. This yields the values for $(1/SF)^4$ 1.66, 2.32, 3.7, 5.96 and when we multiply by the α_0 values we get 76.5 dB/m, 153.6 dB/m, 346.7 dB/m, 428.5 dB/m for the assessment of α near the surface. Because the FBHs lie closer to the back wall, our α assessment seems realistic, but delta α should be greater than zero also for T53 low. In the last assessment, we also did not consider the actual inhomogeneity along the depth axis, which should be a subject of further research.

9 Conclusions

Within this work the detectability of the developed phased array ultrasonic techniques has been investigated on copper tube material with various levels of ultrasonic attenuation.

The investigation has mainly been performed by the use of the multi-parameter POD methodology, which allows several influencing factors to be included. In this work the main parameter has been the varying attenuation in the copper tubes and the main challenge has been to incorporate the physics of the ultrasonic wave in the copper tube material with various and uniform ultrasonic attenuation. The multi-parameter approach is to be preferred for the analysis of phased array ultrasonic focused inspection technique for complex parts, because the POD is a forecast or interpolation means, on the basis of the underlying physical relations, and is most correctly included, when the modelled amplitude is applied for this exact application case. This approach, furthermore, provides with the advantage to include further parameters, such as the depth position or the angle of the defect, in the existing model with much lower experimental effort than producing an empirical POD0 for each parameter setting and varying defect size separately. When the POD is expressed as a function of position within the part, it can be further used for a Volume-POD assessment, used to optimize the coverage of the part, or for data fusion.

The results for the final attenuation are in good agreement with former investigations of the attenuation in copper tubes and the POD results have been verified by conventional POD calculations. The detectable flat bottom hole sizes, as represented by the corresponding d90/95 values, vary from less than 2 mm for low attenuating material up to 4 mm for high attenuating material. This indicates that the developed ultrasonic technique is well suitable for inspection of copper tubes with attenuation up to the level of the investigated material.

In completing the research for heterogeneous attenuation for the future practice in ultrasonic inspection of canister components, a more effective method of using the back wall echo information to determine α and optimum gain for the inspection or even rejection of the tube should be developed, after the basics of physics had been more carefully investigated. In order to verify the specific shape of grain size and frequency dependence of the inhomogeneous copper, additional experiments and mathematical formulations are necessary.

References

ASNT, 1999. Topical conference paper summaries book of the American-European workshop on non-destructive inspection reliability, 21–24 September 1999, NIST, Boulder, Colorado. Columbus, OH: American Society for Nondestructive Testing.

Berens A P, 1989. NDE reliability data analysis. In Metals handbook. 9th ed. Vol 17, Nondestructive evaluation and quality control. Metals Park, OH: ASM International, 689–701.

Boehm R, Brackrock D, Kitze J, Brekow G, Kreutzbruck M, 2009. The SAFT approach for advanced crack analysis. In Proceedings of the National Seminar & Exhibition on Non-Destructive Evaluation, Tiruchirappalli, Tamilnadu, India, 10–12 December 2009. Available at: http://www.ndt.net/article/nde-india2009/pdf/22-C-2.pdf

ENIQ, 2005. ENIQ Recommended Practice 1: Influential/essential parameters. Issue 2. ENIQ Report 24, EUR 21751 EN, European Commission, Directorate General Joint Research Centre (DG JRC), Institute for Energy.

Pavlovic M, Takahashi K, Müller C, Boehm R, Ronneteg U, 2008. NDT reliability – Final report. Reliability in non-destructive testing (NDT) of the canister components. SKB R-08-129, Svensk Kärnbränslehantering AB.

Pavlovic, M, Takahashi K, Ronneteg U, Pitkänen J Müller C, 2009. Multi-parameter influence on the response of the flaw to the phased array ultrasonic NDT system. The volume POD. In Proceedings of the 4th European-American Workshop on Reliability of NDE, Berlin, 24–26 June 2009. Available at: http://www.ndt.net/article/reliability2009/Inhalt/th3a2.pdf

Pavlovic M, Boehm R, Müller C, Pitkänen J, Ronneteg U, 2010. Investigation of the influence of the material attenuation on the POD of the flaws. In Bièth M (ed). Proceedings of the Eight International Conference on NDE in Relation to Structural Integrity for Nuclear and Pressurised Components, Berlin, 29 September – 1 October 2010, 559–568.

Pavlovic M, Takahashi K, Müller C, 2012. Probability of detection as a function of multiple influencing parameters, Insight – Non-Destructive Testing & Condition Monitoring 54, 606–611.

SKB, 2010. Design, production and initial state of the canister. SKB TR-10-14, Svensk Kärnbränslehantering AB.

Stepinski T (ed), Engholm M, Olofsson T, 2009. Inspection of copper canisters for spent nuclear fuel by means of ultrasound. Copper characterization, FSW monitoring with acoustic emission and ultrasonic imaging. SKB TR-09-28, Svensk Kärnbränslehantering AB.

Revision audit trail

Version	Date	Description	Author	Reviewed	Approved
2.0	as first page header	Input values have been corrected and transmission loss recalculated, editorial changes to text section between formula A1-2 and A1-3 in appendix 1, and in figures 6-4, 6-7, 6-13 to 6-24, A1-2 and A1-4 as well as in tables 6-2 to 6-5, 6-7 and 7-1.	T. Heckel P. Brömel M. Pavlovic U. Ronneteg C. Müller	as first page header	as first page header
1.0	2014-01-28	New version	T. Heckel P. Brömel M. Pavlovic U. Ronneteg C. Müller	Sabina Hammarberg (QA) SKBDoc 1422356 (FR)	Jan Sarnet

Appendix 1: Specific Calculation Steps for the Determination of α and POD

In this appendix the procedural steps for the multi-parameter POD analysis is described. The analysis is based on the measured amplitudes from the flat bottom holes with various diameters ranging from 1 to 6 mm from the different test tube segments T53low, T53high, T58high, T64high at the depth of 49 mm were taken as the $\hat{a}$ (Table 5-2 to Table 5-5 third column).

1. Data censoring
   When there is no available value (defect not detected or value below the recording threshold) then the values are censored to be positioned at the maximum noise level or another appropriate value is selected as the recording threshold resulting in the column *Censored Amp* in Table 6-2 to Table 6-5.

2. Calculate attenuation coefficient from the measured BWEs
   First assessment of the attenuation coefficient α in the neighbourhood of the FBH's is done by taking the BWE values from Table 5-2 to Table 5-5, transforming them into dB and then recalculating them into dB/m.

   Formula A1-1

$$\alpha_i = \frac{BWE1_i[dB] - BWE2_i[dB]}{2 \cdot depth_i} \cdot 1000$$

3. Losses by beam spreading and transition loss Cu -> Water
   The next step includes the corrections from beam spreading (modelled BWEs from table 5-13)

   Formula A1-2

$$\alpha_i = \frac{BWE1_i[dB] - BWE2_i[dB] + VT + SK_i}{2 \cdot depth_i} \cdot 1000$$

where VT is the transition loss difference between the second and the first BWE of about 0.75 and SKi is the difference in beam spreading between the first and the second BWE taken from the calculation at 54mm and 108mm. The value in dB/m is then converted to Np/mm for application to the linear amplitude scale.

Formula A1- 3

$$\alpha\left[\frac{Np}{mm}\right] = \frac{\ln(10)}{20\,000}\ \alpha[\frac{\mathrm{dB}}{\mathrm{m}}]$$

4. First re-normalization (N) of measured and censored values by the point wise α values (Formula 2):

   Formula A1- 4

$$Measval\_ZN_i \leftarrow Censored\ Amp / e^{(-a_i \cdot S)}$$

5. Factor for calibration of modelled values to the experiment (MF).
   The assumption is that the low pass filtering effect is negligible for low α and the modelled ideal curve should follow the first α-renormalized T53low values. The assessment of MF for T53low was done by a least square regression between T53low measured values and the ideal line with respect to MF as variable. The result is presented in Figure 6-5. This represents merely the calibration of the model to the experiment.

The other measurement curves for the T53high, T58high and T64high were also adapted by the model factor. In case of no low pass filtering the α would have been determined already from the first and the second BWE difference and beam spreading correction, transition loss and the curves in $Measval\_ZNM_i$ in Figure 6-5 would already all follow the ideal curve. As discussed above, caused by

the low pass filtering effect from the surface to the back wall, a $\Delta\alpha$ (D), as indicated in Figure 6-2, is remaining for each tube segment

The following step includes determining the $\Delta\alpha$ by fitting the modelled $a \cdot MF \cdot e^{-(\alpha 0 + \Delta\alpha)}$ to each set of measured values. The fit is done using a least square approach for the difference of logarithms of measured and modelled values with respect to $\Delta\alpha$. The initial situation and the results after the fit are presented in Figures A1-1 to Figure A1-6

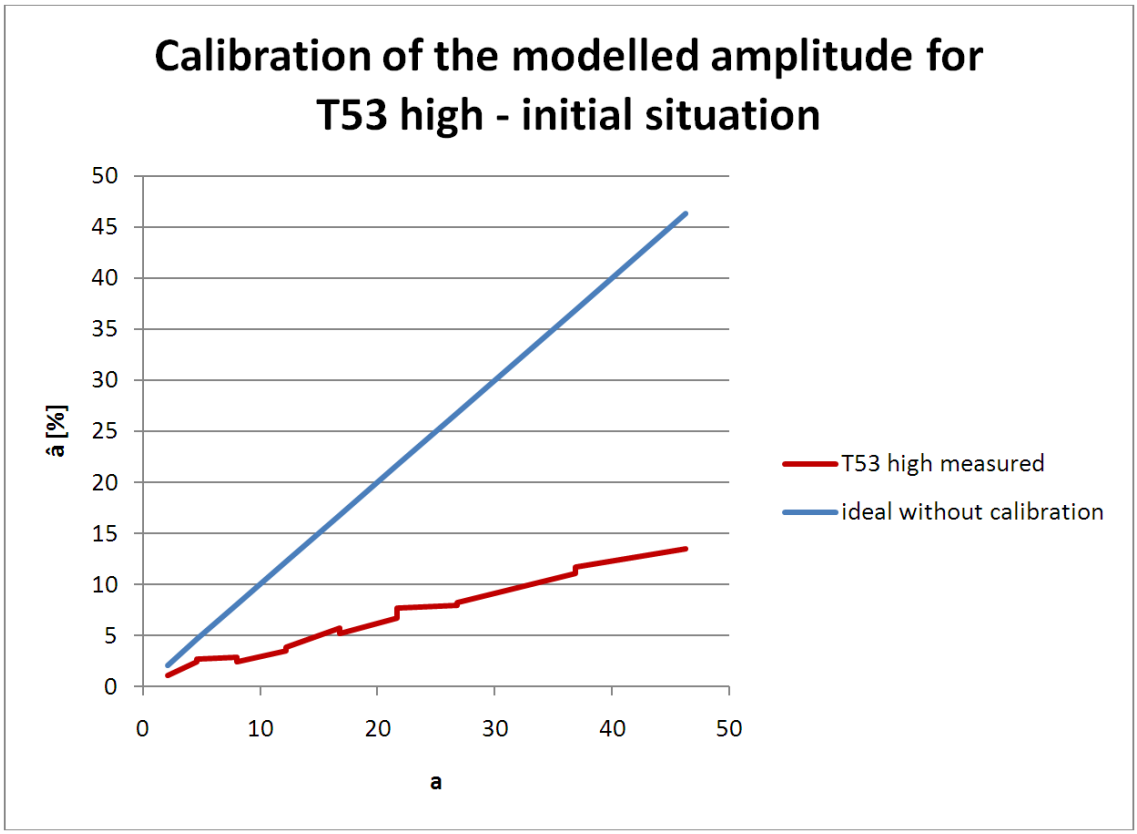

Figure A1-1. *Calibration of the modelled amplitude for T53 high - initial situation.*

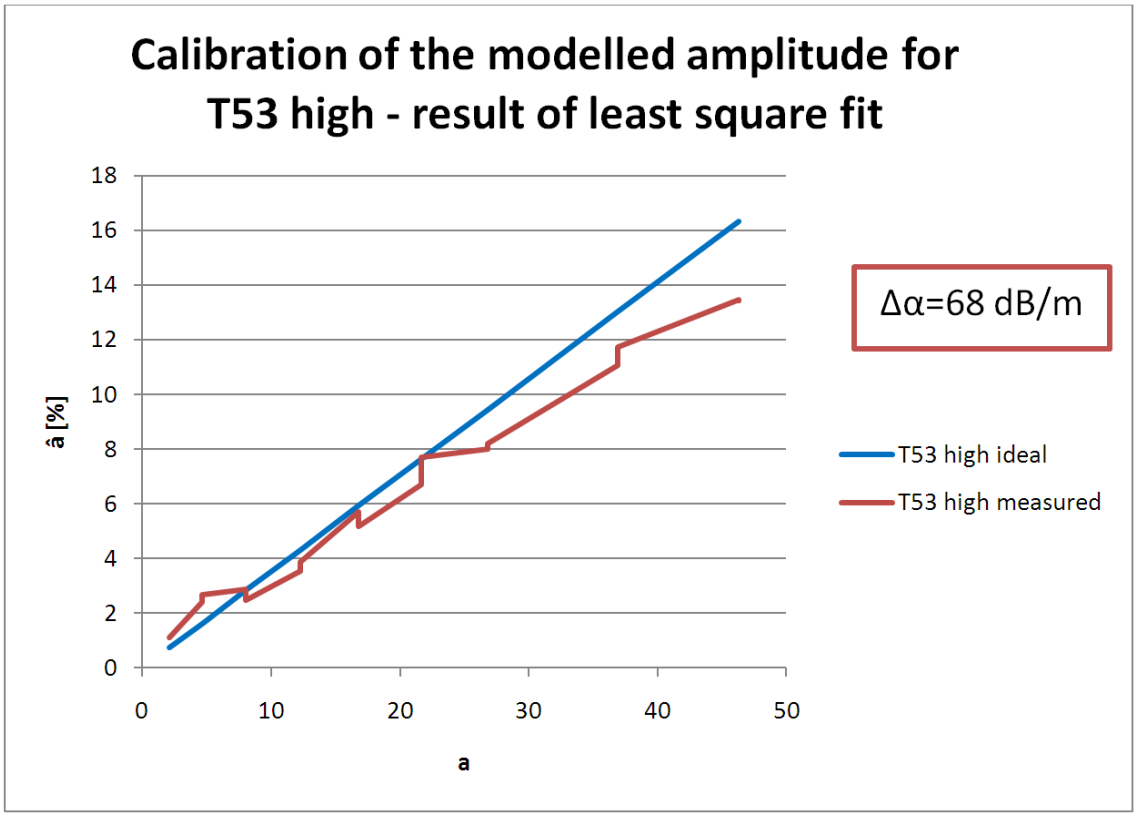

Figure A1-2. *Calibration of the modelled amplitude for T53 high - result of least square fit.*

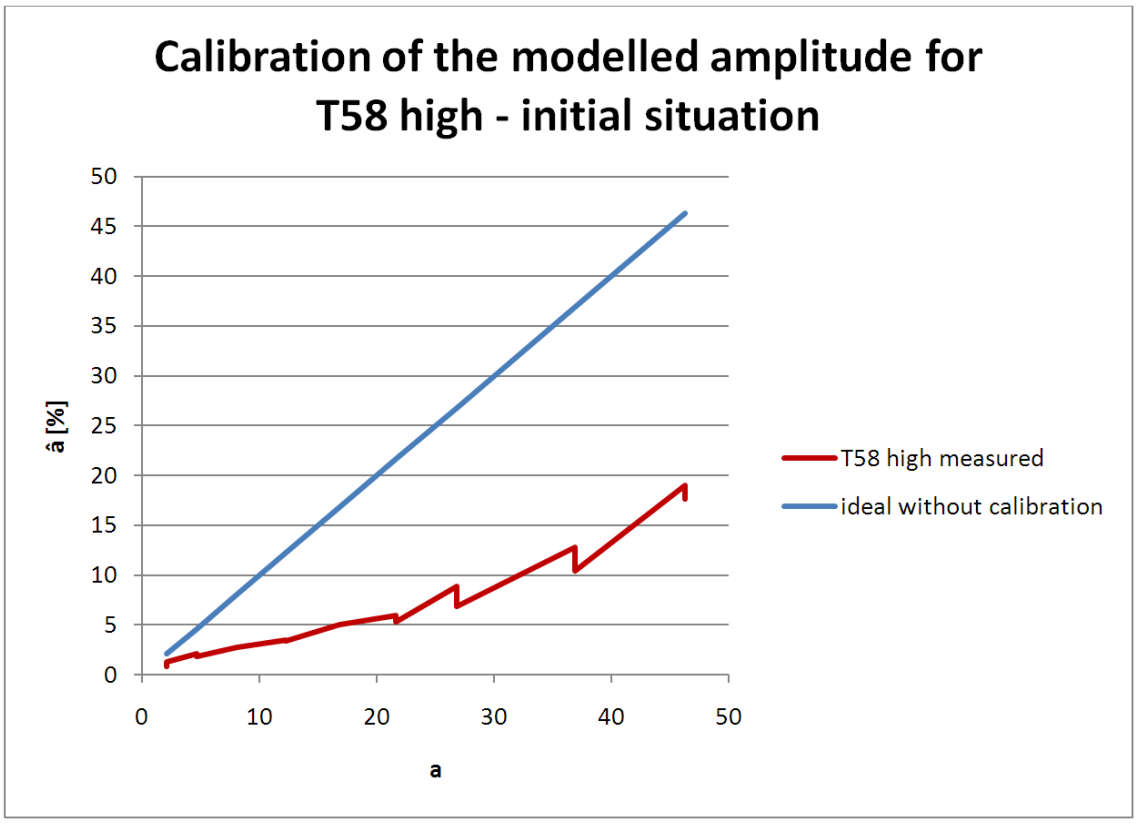

Figure A1-3. *Calibration of the modelled amplitude for T58 high - initial situation.*

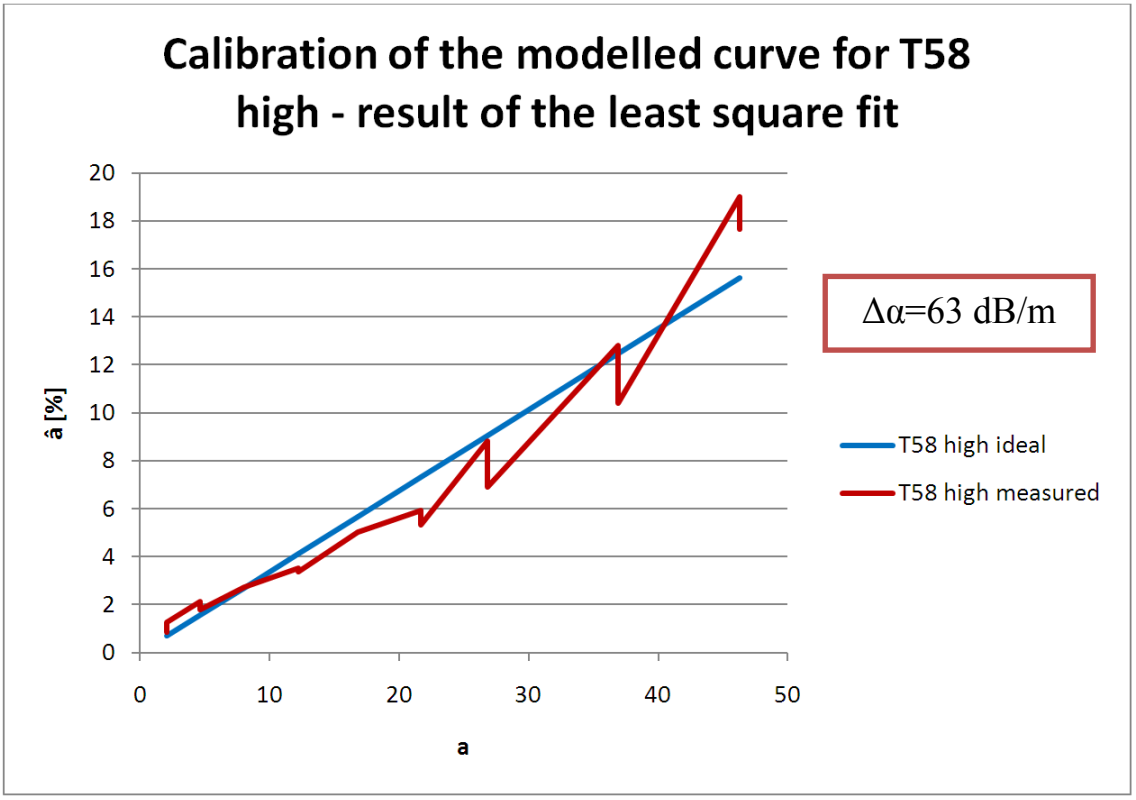

Figure A1-4. *Calibration of the modelled curve for T58 high - result of the least square fit.*

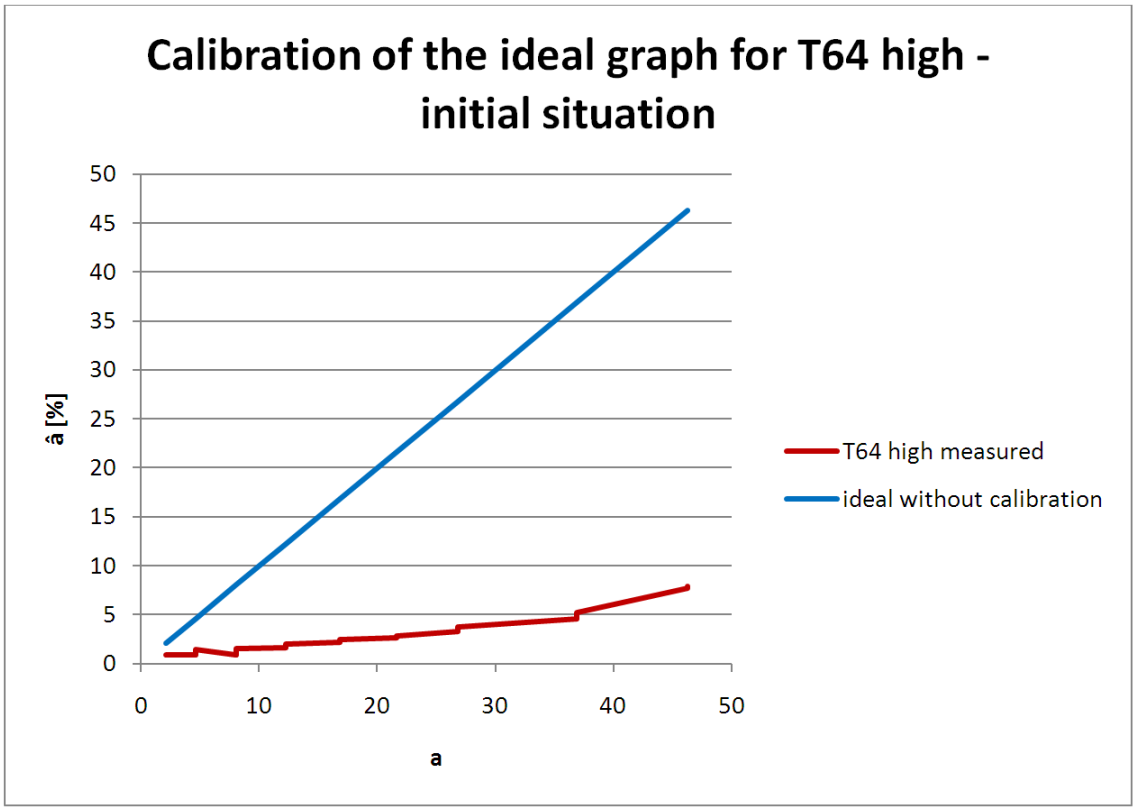

Figure A1-5. *Calibration of the ideal graph for T64 high - initial situation.*

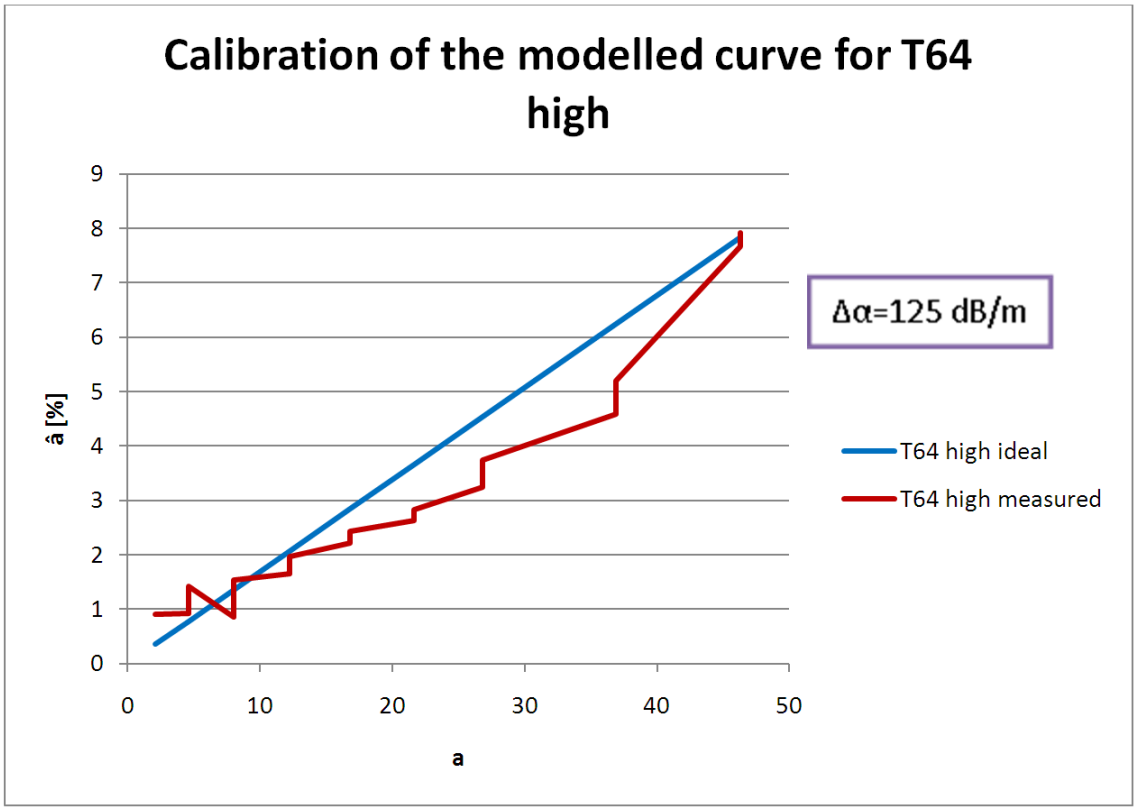

Figure A1-6. *Calibration of the modelled curve for T64 high - result of the least square fit.*

Using the *Δα* values determined above the complete α renormalized measurement values can be created in dividing them, as indicated in formula A1-5.

Formula A1-5

$$Measval\_ZNMD_i \leftarrow Censored\ Amp \ / MF \cdot e^{(-(\alpha + \Delta\propto[\%])_i \cdot S)}$$

The result shown in Figure 6-6 represents the α-free basis data set of the multi-parameter *â versus a.*

The modelled amplitudes will be handed over as *a* and the renormalized measurement values as *â* to the MatLab POD-programme and create the *â* versus *a* regression line using the recording threshold (max noise or otherwise selected), the decision threshold (three times mean noise level) and a saturation threshold (100% screen height)

In order to create the multi-parameter assessments for *α-min*, *α-med* and *α-max* the so called *α* free data set can be scaled by the attenuating factor

Formula A1-6

$$new\ â \leftarrow â(alpha\ free) \cdot e^{(-\alpha \cdot S)}$$

Formula A1-7

$$new\ a \leftarrow a(alpha\ free) \cdot e^{(-\alpha \cdot S)}$$

The new sets *(a, â)* are used to calculate the POD curves for the various attenuations (in practice this means they are handed over to the MatLab POD program).